Astronomy & Astrophysics manuscript no. output
February 10, 2020

Spectral modelling of Type IIb Supernovae.

Comparison to SN 2011dh and the effect of macroscopic mixing.

M. Ergon[1] and C. Fransson[1]

The Oskar Klein Centre, Department of Astronomy, AlbaNova, Stockholm University, 106 91 Stockholm, Sweden

To be submitted to Astronomy and Astrophysics.

ABSTRACT

We use the new NLTE spectral synthesis code JEKYLL to evolve a macroscopically mixed ejecta model of a type IIb SN through the photospheric and nebular phase. The model corresponds to a 12 $M_\odot$ star that have lost most of its hydrogen envelope, and where the ejecta have been strongly mixed in the explosion. The model was previously evolved through the nebular phase with the SUMO code, showing a good agreement with observations of SN 2011dh. Using JEKYLL, we find that the model quite well reproduce both the photospheric and nebular phase SN 2011dh, although there are also some differences. Our work complement and advance earlier work on SN 2011dh, and further strengthens the evidence that this SN originated from a ∼12 $M_\odot$ star. We also investigate the effects of the macroscopic mixing by comparing macroscopically and microscopically mixed models, and by varying the geometrical configuration of the clumps, which is determined by the expansion of clumps containing radioactive material and the typical size of the clumps. In the nebular phase, we find strong effects on the collisional cooling rates in the macroscopically mixed regions, which affects the strength of lines driven by collisional cooling. In particular, the 7291,7323 Å line is much weaker and the [O I] 6300,6364 Å, line much stronger in the macroscopically mixed case. In the photospheric phase, we find strong effects on the opacity in the macroscopically mixed regions, which affects the observed lightcurves. The diffusion peak is considerably narrower in the macroscopically mixed case, and differs strongly if the clumps containing radioactive material in the helium envelope are assumed to expand more than in our standard model. The effect is mainly geometrical, and is driven by the expansion of the clumps containing radioactive material, which creates a density contrast between these and other clumps. As we show, in a uniform radiation field, this allways tends to decrease the effective opacity in the limit of opactically thick clumps. Assuming a uniform opacity that is unaffected by the expansion, the decrease can be quantified as $R = (1 - \Phi_E)^2/(1 - \Phi_E/f_E) + \Phi_E\ f_E$, where Φ_E is the filling factor and f_E the expansion factor of the clumps. This shows that a strong effect can be achieved for a wide range of parameters. The effect also depends on the typical clumps size, as the geometrical part disappears when the clumps becomes optically thin. Our findings has implications for lightcurve modelling of Type IIb SNe, as well as stripped-envelope SNe in general, and the demonstrated effect on the effective opacity will tend to increase the estimated ejecta masses. As was shown in earlier work, a full NLTE solution is required to reproduce the lightcurves and spectra of Type IIb SNe, and it is now clear that *both* NLTE and macroscopic mixing are essential ingredients to reproduce the lightcurves and spectra of Type IIb SNe throughout their evolution.

Key words. supernovae: general

1. Introduction

Type IIb SNe are thought to originate from stars that have lost most, but not all of their hydrogen envelope. Except for the prototypical Type IIb SN 1993J, the most well-observed Type IIb SN is 2011dh, for which we presented observations and modelling of the lightcurves in Ergon et al. (2014, 2015, hereafter E14, E15), as well as modelling of nebular spectra in Jerkstrand et al. (2015, hereafter J15). The modelling suggested a mass of ∼12 $M_\odot$ for the progenitor, a conclusion supported by observations of the star in pre-explosion images (Maund et al. 2011). As stellar winds for stars of this mass seem too low to expel the hydrogen envelope this suggests a binary origin, where the hydrogen envelope was lost through interaction with a companion star. A similar conclusion, based on modelling of the SN (Shigeyama et al. 1994; Woosley et al. 1994), pre-explosion observations of the progenitor star (Aldering et al. 1994), as well as a likely post-explosion detection of the companion star (Maund et al. 2004; Fox et al. 2014), applies to SN 1993J. We also studied a large sample of Type IIb SNe using a grid of hydrodynamical models in Ergon (2015), where we found most of those to originate from relatively low-mass stars. However, the simplified treatment of the opacity in the hydrodynamical modelling, makes this result somewhat uncertain.

Mixing of the SN ejecta occurs in the explosion due to hydrodynamical instabilities (e.g. Mueller et al. 1991). Hydrodynamical modelling suggests that it is extensive in Type IIb SNe (Wongwathanarat et al. 2017), which is supported by observations (e.g. E15), and both theoretical arguments (e.g. Fryxell et al. 1991), and observations (e.g. Ennis et al. 2006) suggests that it occurs on macroscopic scales only. Such *macroscopic mixing* is purely geometrical, and on the microscopic scale the composition remains intact. This in contrast to *microscopic mixing*, which occurs on microscopic scales, e.g. through diffusion or turbulence. In traditional 1-D codes, macroscopic mixing can not be simulated. In that case the choice is to either ignore the mixing or assume that it is microscopic. In MC-based 1-D codes, on the other hand, it is possible to simulate macroscopic mixing in a statistical way, e.g. by using the virtual cell method (Jerkstrand et al. 2011, hereafter J11), which allows for a statistical representation of ejecta consisting of clumps of different composition. JEKYLL supports the virtual cell method, and we can

therefore take the macroscopic mixing of the ejecta into account, and investigate the effects of it. The geometrical configuration of the clumps are, however, not only determined by the fragmentation and mixing that occurs in the explosion, but also by the subsequent expansion of clumps containing radioactive material due to heating from radioactive decays (e.g Herant & Benz 1991).

In this paper we use JEKYLL (Ergon et al. 2018, hereafter E18) to evolve a macroscopically mixed Type IIb model through the photospheric phase and well into the nebular phase. This model belongs to a set of models that was earlier evolved through the nebular phase using SUMO (J11), and compared to the observed nebular spectra and lightcurves of SN 2011dh in J15 and E15, respectively. Out of those, the strongly mixed 12 $M_\odot$ model explored here, showed the best agreement with the nebular spectra and lightcurves of SN 2011dh. It is therefore of great interest to investigate how well this model compares to the spectra and lightcurves of SN 2011dh in the photospheric phase, which is the first objective of this paper. The second objective is to investigate the effects of the macroscopic mixing on the result, and we have therefore constructed a microscopically mixed version of the model, and a set of macroscopically mixed models differing in the geometrical configuration of the clumps. In our treatment, the geometrical configuration is determined by the size of the clumps and their filling factor (the total volume they occupy). The filling factor is in turn determined by the expansion of the clumps containing radioactive material, which creates a density contrast between the clumps.

The paper is organized as follows. In Sect. 2 we describe the ejecta model, the atomic data and the configuration of JEKYLL, in Sect. 3 we discuss the modelling results for our standard model, and compare to observations of SN 2011dh, and in Sect. 4 we investigate the effect of macroscopic mixing on the modelling results. Finally, in Sect. 5 we conclude and summarize the paper.

2. Ejecta models and configuration of JEKYLL

In J15 a set of Type IIb ejecta models differing in initial mass and mixing (as well as other parameters; see J15) were presented. In this paper we explore model 12C, which corresponds to a progenitor star with an initial mass of 12 $M_\odot$ model and strong macroscopic mixing of the ejecta. We construct a standard model, which differs slightly from the original one, and a set of models that differs in the type of mixing (macroscopic or microscopic) and the geometrical configuration of the clumps. Below we repeat the basic properties of model 12C, and describe how our set of ejecta models differ from this model. We also describe the initial conditions, the configuration of JEKYLL and the atomic data used to evolve our models through the photospheric phase into the early nebular phase.

2.1. Ejecta models

A full description of model 12C is given in J15, but we repeat the basic properties here. It is based on a SN model by Woosley & Heger (2007) for a star with an initial mass of 12 $M_\odot$, from which the masses and abundances for the carbon-oxygen core and the helium envelope have been adopted. The carbon-oxygen core is assumed to have a constant (average) density, and the helium envelope to have the same (average) density profile as the best-fit model for SN 2011dh by Bersten et al. (2012). In addition, a 0.1 $M_\odot$ hydrogen envelope based on models by Woosley et al. (1994) is attached. The velocities of the interfaces between the carbon-oxygen core, the helium envelope and the hydrogen envelope are set to 3500 and 11000 km s^{-1}, respectively, based on observations of SN 2011dh.

Based on the original onion-like nuclear burning structure, five compositional zones (O/C, O/Ne/Mg, O/Si/S, Si/S and Fe/Co/He) were identified in the carbon-oxygen core, two (He/N and He/C) in the helium envelope, and one (H) in the hydrogen envelope (see J15 for details). To mimic the mixing of the compositional zones in the explosion, two scenarios with different degrees of mixing (medium and strong) were explored in J15. The model explored here (12C) has strong mixing, corresponding to a fully mixed carbon-oxygen core and about half of the radioactive Fe/Co/He material mixed into the inner part of the helium envelope.

As in J15 we take the macroscopic nature of the mixing into account using the virtual cell method (J11). However, here we use this method also in the helium envelope, where J15 used alternating shells to represent the mixing. Although the alternating shell method catch the effect of the different density and composition in the clumps on the matter state, it can not catch the effect of the geometrical configuration of the clumps on the radiative transfer, and as we will see this effect is important. We also differ from J15 in that we use the same mass of all clumps, which seems more physically sound than using the same number of clumps for each nuclear compositional zone. The clump mass is set to give the same number of clumps in the core as in the original J15 model.

In the J15 model, the Fe/Co/He and Si/S clumps are assumed to expand with a factor of 10 in the carbon-oxygen core due to heating from the radioactive decays (which results in a corresponding compression of the other clumps). However, this is not assumed to happen with the Fe/Co/He clumps mixed into the helium envelope. Although it is uncertain how much these clumps expand (in particular in the helium envelope), we find it more reasonable to assume that they expand also in the helium envelope. In our standard model we assume that they expand with a factor of five, half as much as in the core, and therefore deviate from the original J15 model in this respect.

To explore the effects of macroscopic mixing we have constructed a microscopically mixed model, 12C-micro, by just averaging the abundances, and a set of macroscopically mixed models that differs in the expansion of the Fe/Co/He and Si/S clumps and the size of the clumps. All models, and their parameters, are listed in Table 1. The standard model 12C-macro-he-exp-5, which is used in the comparison with SN 2011dh, is the same as the original J15 model except that the Fe/He/Co clumps in the helium envelope has been expanded with a factor of 5. Model 12C-macro-no-exp differs in that the Fe/He/Co and Si/S clumps have not been expanded at all, and model 12C-macro-he-exp-8.5 in that the F/He/Co clumps in the helium envelope have been expanded with a larger factor (8.5). Finally model 12C-macro-he-exp-8.5-x100 is the same as model 12C-macro-he-exp-8.5, except that the number of clumps has been increased with a factor of 100 (corresponding to $10^{3/2}$ times smaller clumps).

2.2. Initial conditions

As for the HYDE models in E15, the initial temperature profile was taken from the best-fit hydrodynamical model for SN 2011dh from that paper. This SN model was based on a bare helium core model, and therefore the cooling of the thermal explosion energy, lasting for a few days in a model with a hydrogen envelope, is ignored. The subsequent evolution is powered by the continuous injection of radioactive decay energy, and the

Table 1. Ejecta models.

Name	Type of mixing	Fe/He/Co expansion core	Fe/He/Co expansion envelope	Clump mass ($M_\odot$)
12C-mic	microscopic	-	-	-
12C-mac-he-exp-5	macroscopic	10	5	8.4×10^{-6}
12C-mac-no-exp	macroscopic	1	1	8.4×10^{-6}
12C-mac-he-exp-8.5	macroscopic	10	8.5	8.4×10^{-6}
12C-mac-he-exp-8.5-x100	macroscopic	10	8.5	8.4×10^{-8}

choice of initial temperature profile is not critical, although it may have some effect on the early evolution.

2.3. Configuration of JEKYLL

JEKYLL was configured to run in time-dependent (radiative transfer) mode, and to use a full NLTE solution including the following; radiative bound-bound, bound-free and free-free processes, collisional bound-bound and bound-free processes, non-thermal excitation, ionization and heating, as well as two-photon processes. JEKYLL was also configured to use the diffusion solver below an optical depth of 50, and a recombination correction while still enforcing detailed balance. In addition, packet control (E18) was turned on to assure good sampling of the radiation field in all frequency regions. The logarithmic time-step was set to 5 percent and the number of Λ-iterations per time-step was set to 4. As discussed in E18, this gives a well converged solution, which has also been verified for the models used in this paper.

2.4. Atomic data

The atomic data used is the same as for the microscopically mixed Type IIb model presented in E18, but has been extended with more levels and a full NLTE solution for ionization stage VI and V. This make only a small difference for the observed lightcurves and spectra, but is needed to study the opacity in the macroscopically mixed core, which becomes very hot at early times. Using online data provided by NIST[1] and R. Kurucz[2], these ions where updated to include 100 levels (or as many as were available) for elements lighter than SC, and 300 levels (or as many as were available) for heavier elements. Total recombination rates for these ions were adopted from the online table provided by S. Nahar[3] whenever available, and otherwise from Shull & van Steenberg (1982).

3. Comparisons with observations

Among the Type IIb models presented in J15, model 12, which has an initial mass of 12 $M_\odot$ and strong mixing was found to give the best match to the observed nebular spectra (J15) and lightcurves[4] (E15) of SN 2011dh. It is therefore of great interest to explore how well this model reproduces the early spectra and lightcurves, something which is now possible using JEKYLL. In addition, it is also interesting in itself to run a self-consistent model from the photospheric to the nebular phase, although we expect to get a good match in nebular phase as JEKYLL compared well with the SUMO in E18. Note, that we here use our standard version of model 12C, which differs from the original one in that the Fe/Co/He clumps in the helium envelope are expanded with a factor of 5 (see Sect. 2.1).

In Sects. 3.1, 3.3, 3.4 and 3.5 we discuss the spectral, photometric, colour and bolometric evolution of the standard model and compare to observations of SN 2011dh. We also discuss the physical processes giving rise to the observed evolution and in Figs. 1 we show the evolution of the temperature, electron fraction, radioactive energy deposition and photosphere of the model.

3.1. Spectral evolution

Figures 2 and 3 show the spectral evolution for the standard model between 0 and 150 days, where the former figure displays the process, and the latter figure the location giving rise to the emission[5]. Furthermore, in Fig. 4 we compare the spectral evolution in the optical and near-infrared (NIR) to observations of SN 2011dh. As seen in Fig. 4, there is a good qualitative, and in many aspects also quantitative agreement, between the standard model and the observations of SN 2011dh. Before ~10 days, when the emission comes mainly from the hydrogen envelope the agreement is a bit worse (not shown). This is possibly an effect of the choice of initial conditions for the model (see Sect. 2.1), where the initial cooling of the explosion energy, lasting a few days, has been ignored.

The main signature of a Type IIb SN is the transition from a hydrogen to a helium dominated spectrum, and this is well reproduced by the model. Initially, the hydrogen lines are strong and emission from the hydrogen envelope is dominating. Already at ~10 days emission from the helium envelope starts to dominate redwards ~5000 Å, and between 10 and 15 days the helium lines appear, grow stronger, and eventually dominate the spectrum at ~40 days. Hydrogen line emission disappears on a similar time-scale, completing the transition, although the Balmer lines remain considerably longer in absorption. The first 40 days is also the period over which the contribution from continuum processes fades away. Initially, this contribution is substantial redwards ~5000 Å and dominating in the NIR, but then quickly fades away although it remains important in the *H*-band and redwards 23000 Å until ~40 days.

After ~40 days, emission from the carbon-oxygen core becomes increasingly important and at ~100 days it dominates redwards ~5000 Å. As a consequence, emission from heavier elements abundant in the core increases, in particular after ~100 days, when the characteristic [O I] 6300,6364 Å and [Ca II] 7291,7323 Å lines appear. This is also the moment when the

[1] www.nist.gov
[2] http://www.cfa.harvard.edu/amp/ampdata/kurucz23/sekur.html
[3] http://www.astronomy.ohio-state.edu/~nahar/_naharradiativeatomicdata/
[4] The best match was found for model 12F, which differs from model 12C only in the optical depth of the dust.
[5] Based on the last emission events for the MC packets excluding electron scattering.

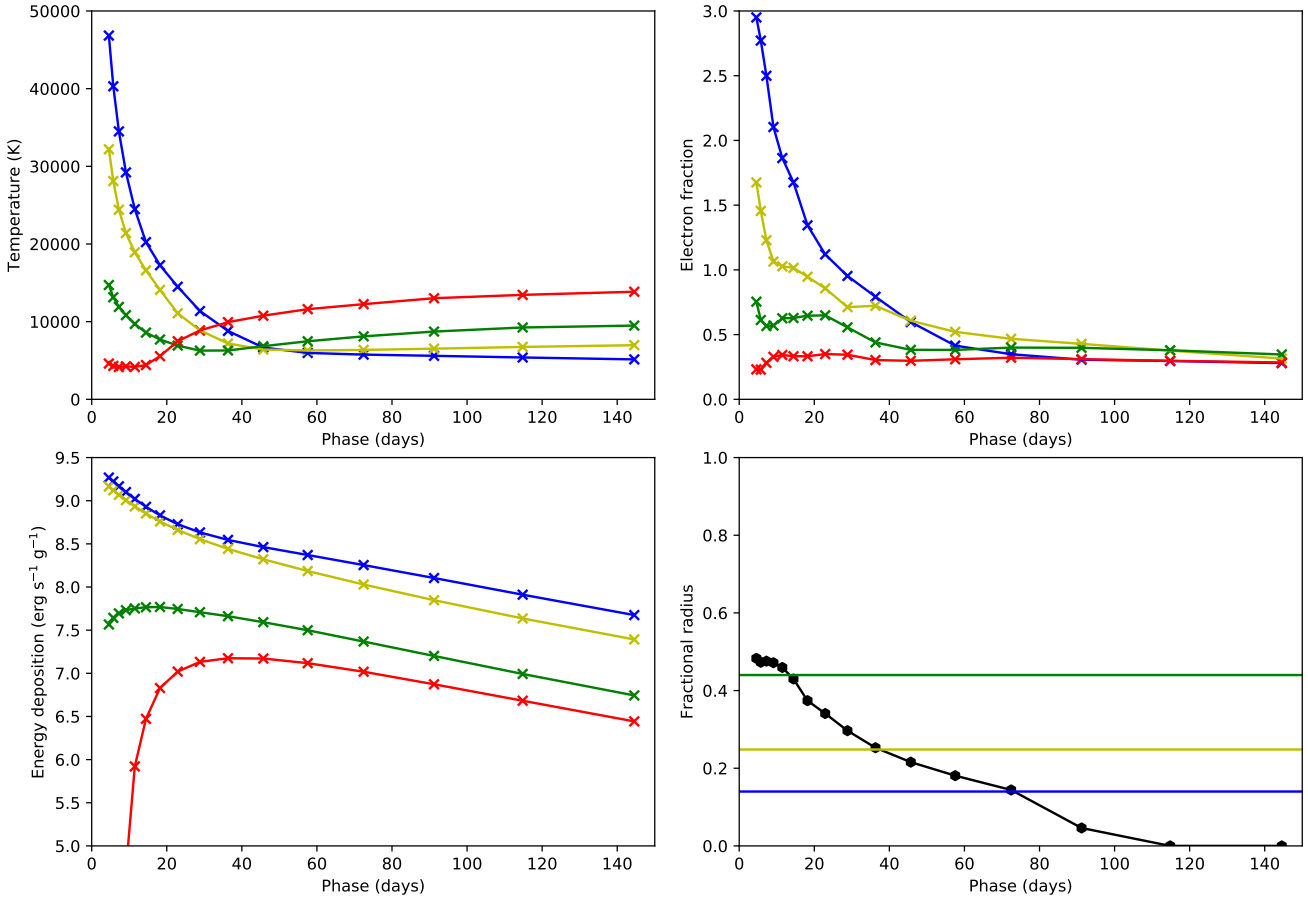

Fig. 1. Evolution of the temperature (upper left panel), electron fraction (upper right panel) and radioactive energy deposition (lower left panel) in the oxygen core (blue), inner/outer (yellow/green) helium envelope and the hydrogen envelope (red) for the standard model. In the lower right panel we show the evolution of the (Rosseland mean) continuum photosphere as well as the outer borders of the carbon-oxygen core (blue) and inner/outer (green/yellow) helium envelope.

carbon-oxygen core becomes fully transparent in the continuum (see Fig.1), and therefore marks the transition into the nebular phase. This transition, in itself a demanding test of the code, is quite nicely reproduced by the model. As discussed in Sect. 4, this is partly due to our treatment of the macroscopic mixing.

Below, we discuss the most important lines originating from the different elements in some detail (Sects. 3.1.1-3.1.5), as well as the line velocities measured from their absorption minima (Sect. 3.2.1), and again compare to observations of SN 2011dh.

3.1.1. Hydrogen

The contribution from hydrogen lines is shown in Fig. 2, and as mentioned it is initially strong, but fades away after ∼10 days, when the photosphere retreats into the increasingly transparent helium envelope (see Fig. 1). This trend is most pronounced for the recombination driven Paschen lines, which disappear towards ∼40 days. Balmer line emission fades on a similar timescale, whereas absorption remains for a longer time, and even increases before ∼40 days. Contrary to the other Balmer lines, Hα initially shows a clear P-Cygni profile, but after ∼10 days it becomes increasingly blended with the He I 6678 Å line and attains the double-peaked shape so characteristic in Type IIb SNe.

Figure 5 shows the evolution of the Balmer lines compared to SN 2011dh. The evolution is qualitatively similar, but the absorption is significantly stronger and remains longer in the model, suggesting that the ∼0.05 $M_\odot$ of hydrogen in the model is larger than for SN 2011dh. This is in line with the 0.02-0.04 and 0.024 $M_\odot$ of hydrogen estimated through spectral modelling of SN 2011dh by E14[6] and Marion et al. (2013), respectively. In agreement with the spectral modelling in E14, we also find that the absorption minimum of the Balmer lines asymptotically approaches the velocity of the helium/hydrogen envelope interface. The Type IIb models by Dessart et al. (2015, 2016) behave in a similar way, and a stagnation of the absorption velocity for the Balmer lines is observed in most Type IIb SNe (see e.g. Liu et al. 2016). The stagnation velocity varies among different SNe, and for the most well-observed Type IIb SNe 1993J, 2011dh and 2008ax it is ∼9000, ∼11000 and ∼13000 km s^{-1} respectively, suggesting progressively lower hydrogen masses for these SNe (E14).

3.1.2. Helium

The contribution from helium lines is shown in Fig. 2, and as mentioned it increases strongly between 10 and 15 days, dominates the spectrum between 20 and 60 days and thereafter fades away in the optical, but remains important in the NIR. As demonstrated by Lucy (1991), non-thermal excitation and ion-

[6] Using an early version of JEKYLL assuming steady-state, LTE and (electron and line) scattering only.

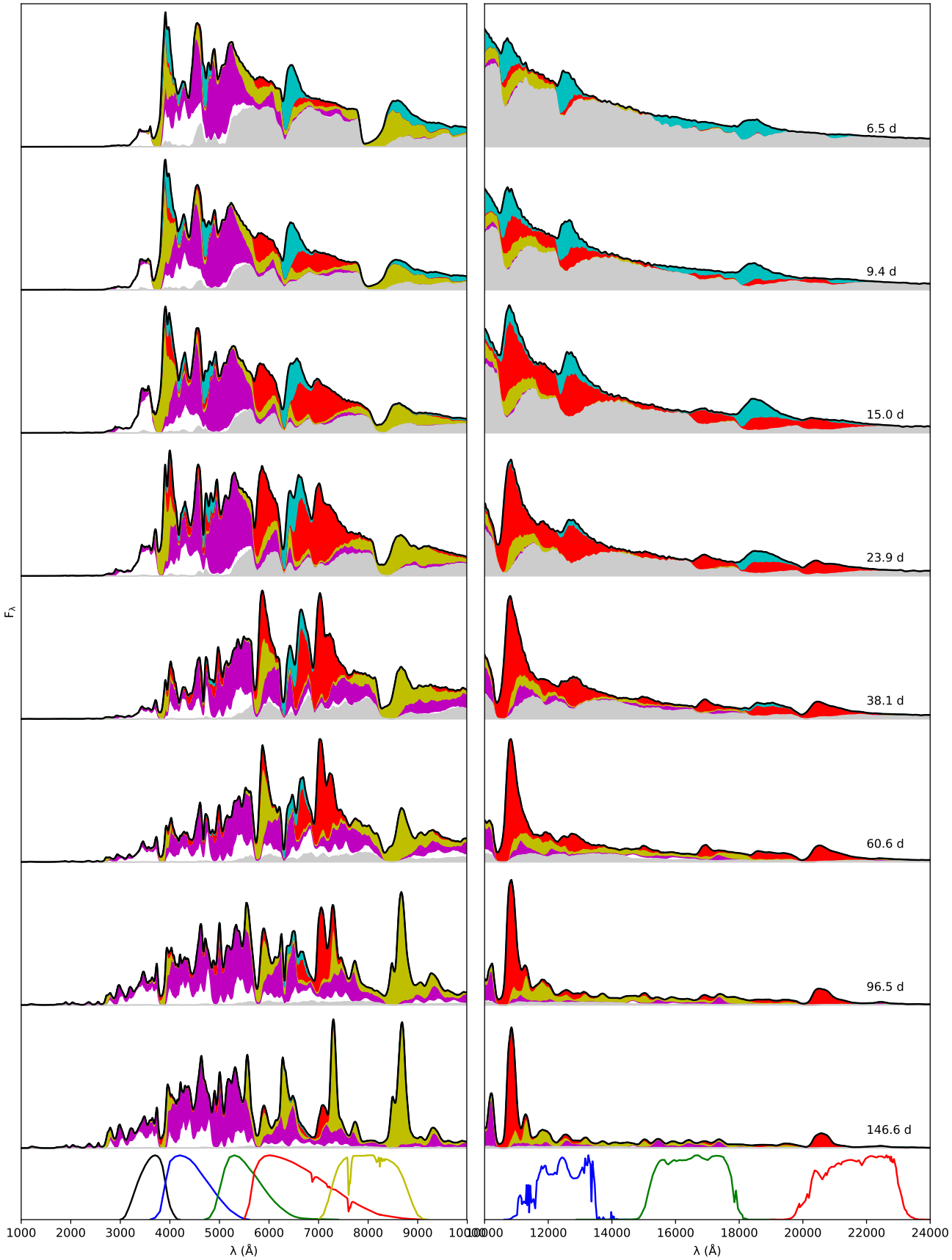

Fig. 2. Spectral evolution in the optical (left panel) and NIR (right panel) for the standard model. In the spectra we show the contributions to the emission from bound-bound transitions of hydrogen (cyan), helium (red), carbon-calcium (yellow), scandium-manganese (white) and iron-nickel (magenta) as well as continuum processes (grey). At the bottom we show the transmission profiles of the optical Johnson-Cousins *U* (black), *B* (blue), *V* (green), *R* (red) and *I* (yellow) bands and the NIR 2MASS *J* (blue), *H* (green) and *K* (red) bands.

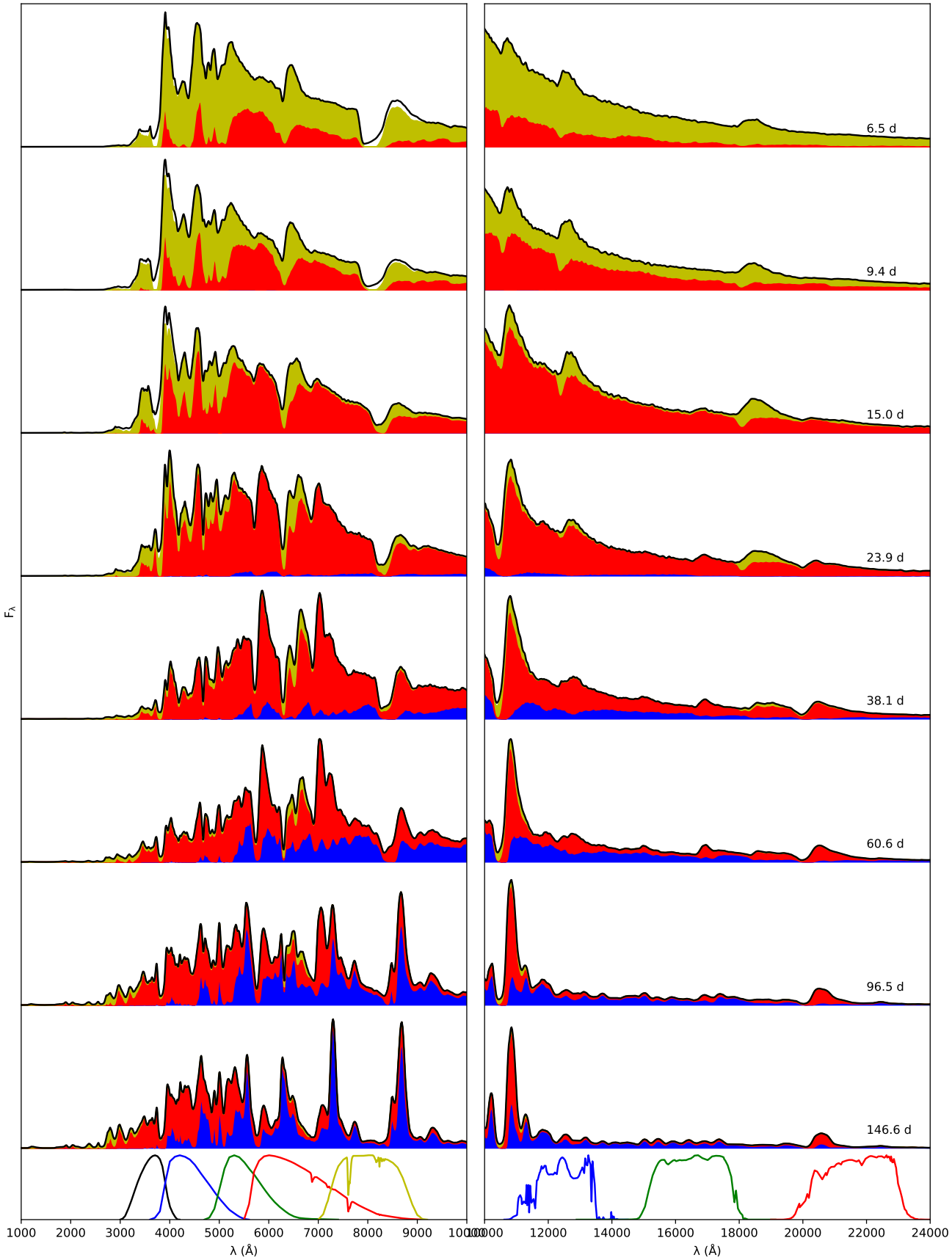

Fig. 3. Spectral evolution in the optical (left panel) and NIR (right panel) for the standard model. In the spectra we show the contributions to the emission from the carbon-oxygen core (blue), and the helium (red) and hydrogen (yellow) envelopes. At the bottom we show the transmission profiles of the optical Johnson-Cousins *U* (black), *B* (blue), *V* (green), *R* (red) and *I* (yellow) bands and the NIR 2MASS *J* (blue), *H* (green) and *K* (red) bands.

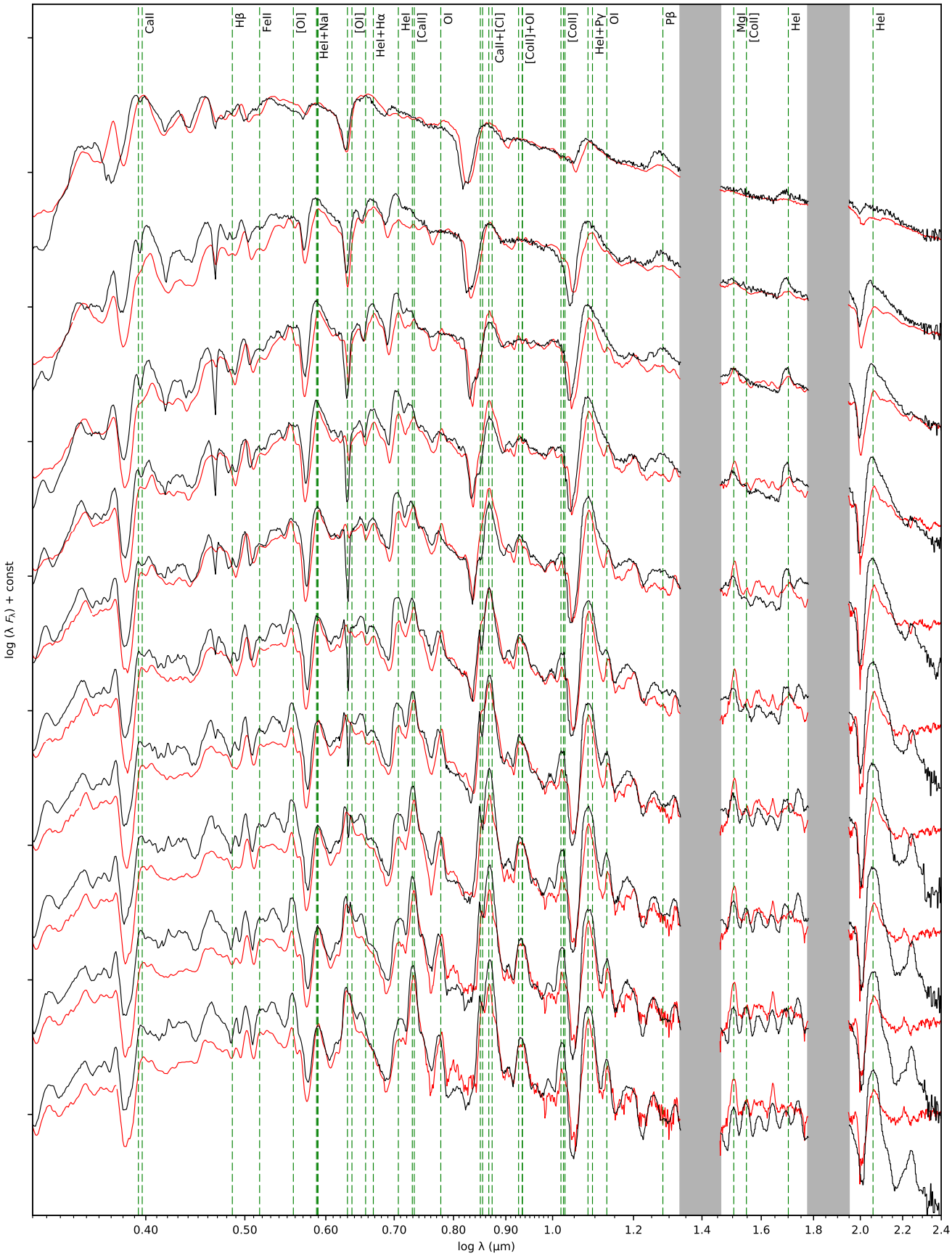

Fig. 4. Spectral evolution for the standard model (black) compared to the observations of SN 2011dh (red). Spectra from 10 equally spaced epochs between 15 and 150 days are shown, where those of SN 2011dh have been interpolated as described in E14. In addition, the rest-wavelengths of the most important lines are shown as red dashed lines and the NIR telluric absorption bands as grey vertical bars.

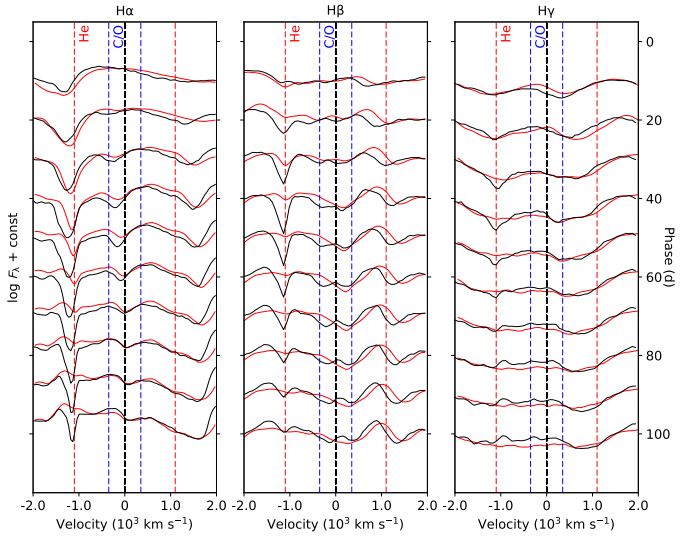

Fig. 5. Evolution of hydrogen lines for the standard model (black) compared to the observations of SN 2011dh (red). Spectra from 10 equally spaced epochs between 10 and 100 days are shown, where those of SN 2011dh have been interpolated as described in E14. Here, as well as in Figs. 6-9, we also show the velocity extent of the helium envelope (red lines) and the carbon-oxygen core (blue lines).

ization are essential to populate the excited levels of He I, in turn required to produce the lines observed. This was confirmed by Dessart et al. (2012), and in E18 we showed that if the non-thermal excitation and ionization was turned off in a microscopically mixed version of the model explored here, the helium lines disappeared.

Figure 6 shows the evolution of the He I 5876 Å, 6678 Å, 7065 Å, 10830 Å, 17007 Å and 20581 Å lines compared to SN 2011dh. These are the lines that stand out most clearly in the model, but several other weaker and blended lines are also present. The He I 5876 Å, 6678 Å and 10830 Å lines are quite well reproduced by the model, whereas the He I 7065 Å and 20581 Å lines are a bit overproduced, and the weaker He I 17007 Å line (mainly seen in emission) is considerably stronger than in the observed spectra. Note, that after ~50 days most of the He I 5876 Å line emission begin to scatter into the Na I 5890,5896 Å line.

As seen in Fig. 6, the He I 10830 Å absorption migrates outward in velocity until ~40 days, a behaviour repeated to some degree in the He I 20581 Å line. This behaviour is also observed in SN 2011dh, although in that case the optical helium lines showed a similar, but less pronounced trend. In E14 we suggested that the evolution of the helium lines is driven mainly by the ejecta becoming optically thin to the γ-rays. This idea is supported by Fig. 7, which shows the evolution of the radioactive energy deposition in the helium envelope. Between 10 and 15 days we see a strong increase in the energy deposition outside the photosphere, corresponding well to the period when the helium lines appear and grow in strength. We also see that the energy deposition in the outermost helium layers continues to increase to ~40 days, which may explain the evolution of the He I 10830 Å line. The outward migration of the He I 10830 Å absorption is also present in the Type I/IIb models (e.g. model 3p65Ax1) by Dessart et al. (2015, 2016), and was noted and discussed by the authors, who also provide a similar explanation.

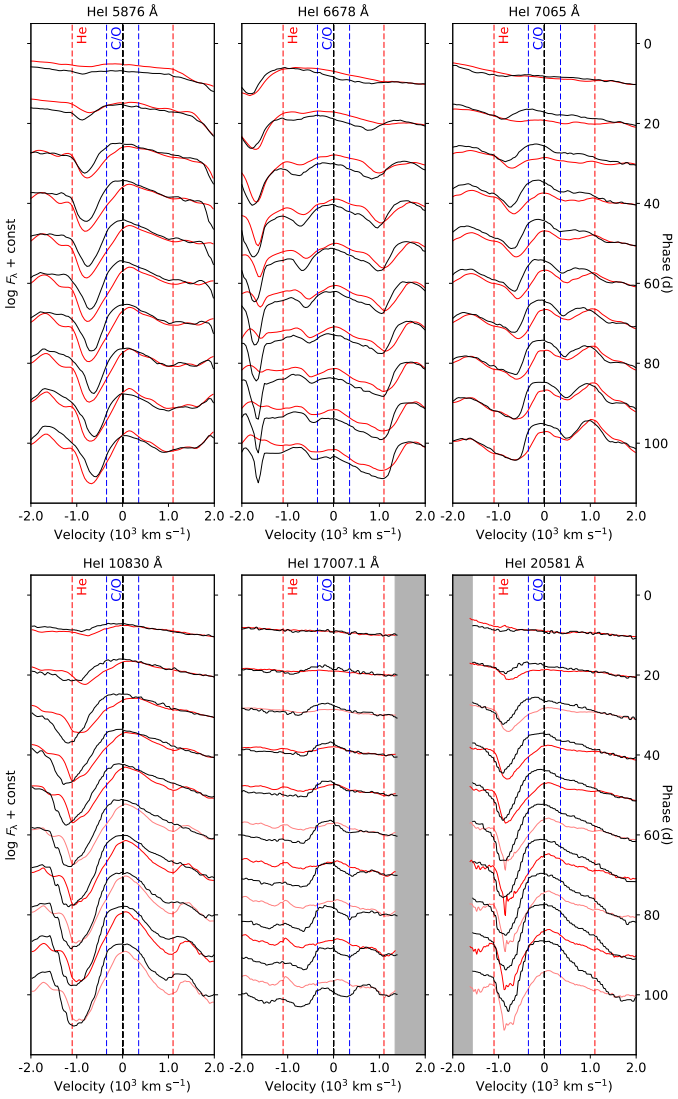

Fig. 6. Evolution of optical (upper panel) and NIR (lower panel) helium lines for the standard model (black) compared to the observations of SN 2011dh (red). Spectra from 10 equally spaced epochs between 10 and 100 days are shown, where those of SN 2011dh have been interpolated as described in E14.

3.1.3. Carbon to calcium

The (line) contribution from elements in the carbon to calcium range is shown in Fig. 2, and except for the calcium lines which are strong at all times, the contribution increases after ~40 days when the core, rich in these elements becomes increasingly transparent (see Fig. 3). The upper panel of Fig. 8 shows the evolution of the Ca II 3934,3968 Å, Ca II 8498,8542,8662 Å and [Ca II] 7291,7323 Å lines compared to SN 2011dh. After ~15 days the evolution of these lines is well reproduced by the model. However, at earlier times absorption in the Ca II 3934,3968 Å and Ca II 8498,8542,8662 Å lines extend further out in the model. Again, this is possibly an effect of the choice of initial conditions.

The lower panel of Fig. 8 shows the evolution of the [O I] 5577 Å, [O I] 6300,6364 Å, O I 7774 Å, O I 11290,11300 Å and Mg I 15040 Å lines compared to SN 2011dh. The evolution of the oxygen lines is fairly well reproduced, but the O I 7774 Å and

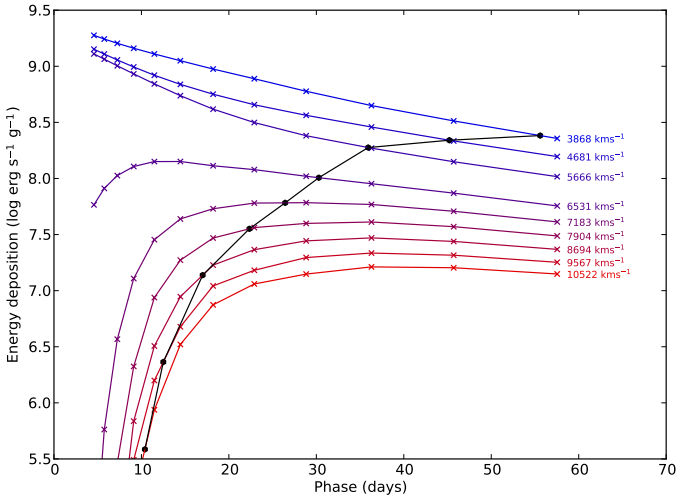

Fig. 7. Evolution of the radioactive energy deposition in the helium envelope (red to blue crosses) and the position of the (Rosseland) continuum photosphere (black circles) for the standard model.

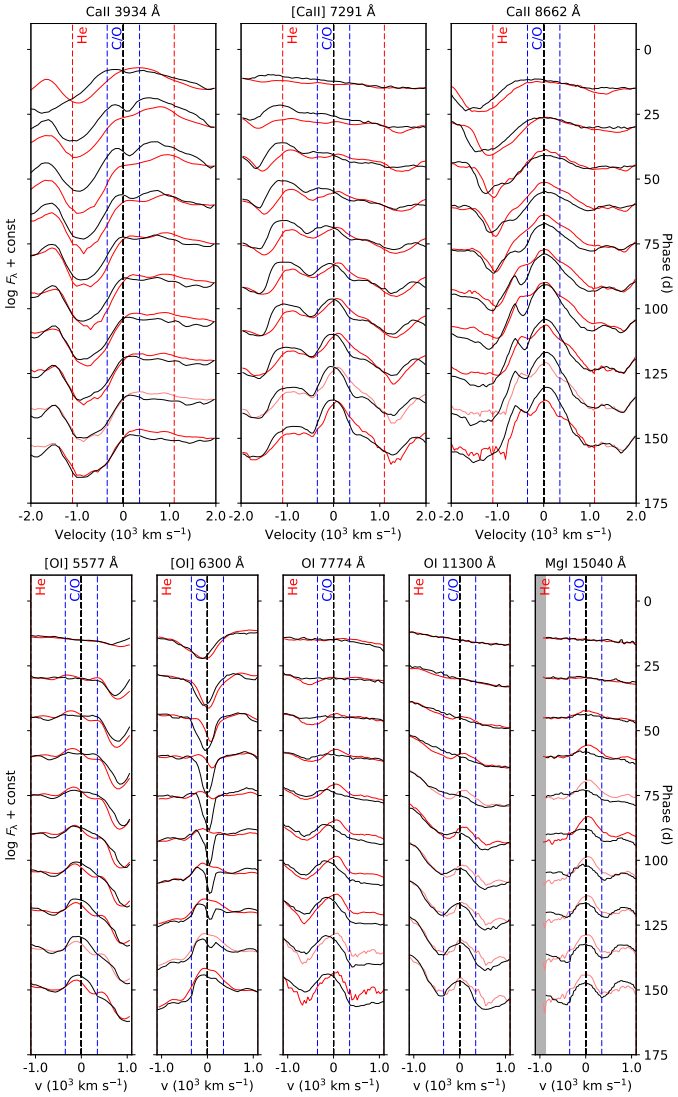

Fig. 8. Evolution of calcium, oxygen and magnesium lines for the standard model (black) compared to the observations of SN 2011dh (red). Spectra from 10 equally spaced epochs between 15 and 150 days are shown, where those of SN 2011dh have been interpolated as described in E14.

11290,11300 Å lines appear later and are initially weaker than observed for SN 2011dh. The O I 9263 Å line is also present in the model but is blended with the [Co II] 9338,9344 Å line (see Sect. 3.1.5).

In the model, the early (near peak) feature at ~9200 Å is mainly caused by the Mg II 9218,9244 Å line, and later the Mg I 15040 Å line appears. The latter is well reproduced in the nebular phase (after ~100 days), but appears later and is initially weaker than observed for SN 2011dh. We note that whereas the radioactive Fe/Co/He material was mixed into the helium envelope, the oxygen and magnesium rich material was not, which may explain the early suppression of several oxygen and magnesium lines compared to observations.

As mentioned in Sect. 3.1.2, the Na I 5890,5896 Å line overtakes He I 5876 Å line at ~60 days, and as seen in Fig. 6 the subsequent evolution is well reproduced. In the model, the feature emerging at ~11800 Å after ~60 days is mainly caused by the C I 11760 Å line, and towards ~150 days the [C I] 8727 Å line begins to contribute significantly to the blend with the Ca II 8498,8542,8662 Å line.

3.1.4. Scandium to manganese

The (line) contribution from elements in the scandium to manganese range is shown in Fig. 2, and is dominating in the 3000-4000 Å region and important in the 4000-5000 Å region at all times. After ~40 days it also contributes significantly to the optical emission redwards 5000 Å. The emission is the result of scattering and fluorescence in numerous transitions, and individual lines are hard to distinguish. Line-blocking by elements in the scandium to manganese range is important for the suppression of the emission bluewards ~5000 Å, and in particular in the 3000-4000 Å region, corresponding roughly to the *U*-band.

3.1.5. Iron to nickel

The (line) contribution from elements in the iron to nickel range is shown in Fig. 2, and this contribution is strong at all times, in particular in the 4000-5500 Å range. After ~40 days the contribution increases also at other wavelengths, likely due to emission from the increasingly transparent core (see Fig. 3), where about half of the Fe/Co/He material resides. Except for the *U*-band (see Sect. 3.1.4), blocking through scattering and fluorescence in numerous iron lines is the main cause for the suppression of the emission bluewards ~5500 Å, so important in shaping the spectra of SE SNe. However, with a few exceptions, like the Fe II 5169 Å line, individual iron lines are typically strongly blended and hard to distinguish. The contribution from nickel is insignificant at all times, but after ~50 days cobalt begins to contribute to the spectrum with several distinct lines.

Figure 9 shows the evolution of the Fe II 5169 Å and [Co II] 9338,9344 Å, [Co II] 10190,10248,10283 Å and [Co II] 15475 Å lines compared to SN 2011dh. The Fe II 5169 Å line is reasonably well reproduced, but initially absorption occurs at higher velocities than observed, a discrepancy that disappears towards 150 days. As mentioned the [Co II] 9338,9344 Å line is blended with the O I 9338,9344 Å line, and this blend is well reproduced

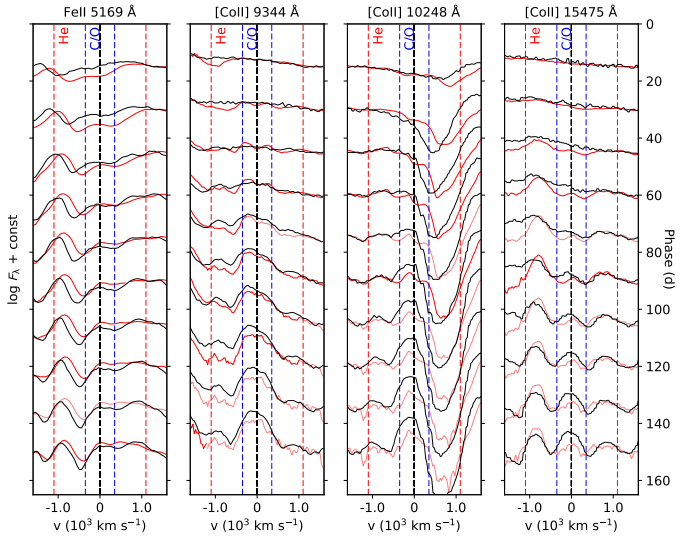

Fig. 9. Evolution of iron and cobalt lines for model the standard model (black) compared to the observations of SN 2011dh (red). Otherwise as in Fig. 8.

by the model. The other [Co II] lines at 10190,10248,10283 Å and 15475 Å are a bit overproduced by the model. The iron and cobalt lines are interesting as they are directly linked to the distribution of the Fe/Co/He material in the ejecta, and the discrepancies seen may indicate that the mixing of this material is different than in the model.

3.2. The infrared spectrum

The near-infrared and mid-infrared spectrum is of special interest because of the relatively isolated lines especially in the nebular phase. Because of their low excitation temperature these lines are also relatively insensitive to temperature and therefore especially suitable for abundance estimates. Several elements, like Ne and Ar, also have some of the few strong lines in this range. The usefulness of this range was demonstrated by the Kuiper Airborne Observatory (KAO) observations of SN 1987A and similar observations of more distant SNe will be possible with the NIRSPEC and MIRI instruments on the James Webb Space telescope (JWST).

In Fig. 24 we show the full spectra at three representative epochs. The IR spectrum at 26 days, close to maximum, is mainly an extension to the optical spectrum, with a few strong He I lines at 1.083, 2.058, 4.2959, and 7.456μm. While the 1.083μm line has a strong P-Cygni absorption the other lines are mainly in emission. At 100 days the IR spectrum is becoming more nebular with strong emission lines from [Ni II] 6.636μm, [Ar II] 6.985μm, [Co II] 10.522μm, and [Co III] 11.883μm.

The last spectrum at 308 days is fully nebular above $\sim$ 2.5μm. There is at this phase only a weak continuum. In the NIR lines of [Fe II] 1.26, 1.53, 1.644 and 1.81 are strong. The line at $\sim$ 1.64μm is, however, a blend of [Si I] 1.646μm and [Fe II] 1.644μm. The MIR lines have luminosities comparable to the optical lines due to the decreasing temperature. In addition to the [Ni II] 6.636μm, [Ar II] 6.985μm, [Co II] 10.522μm, and [Co III] 11.883μm, which are strong at 100 days, also [Ne II] 12.814μm, [Fe II] 17.936, 24.519, 25.988, 35.772μm, [Fe III] 22.925, 33.038μm, [Co II] 10.522μm, and [Co III] 11.883μm are now strong.

Most of the lines correspond to fine-structure transitions in the ground state multiplets, which are close to be in LTE. They are therefore sensitive to the ionization fractions of the ions and elemental abundances, but less so to the temperature (as $kT/h\nu$ is usually small).

3.2.1. Line velocities

Figure 11 shows the velocity evolution of the absorption minima of the Hα, Hβ, He I 5876 Å, He I 6678 Å, He I 10830 Å, He I 20581 Å, O I 7774 Å and Fe II 5169 Å lines, as well as the (Rosseland mean) continuum photosphere (compare; E15: Fig. 14). The hydrogen lines show the highest velocities, have a flat evolution, and as discussed (Sect. 3.1.1), they approach the velocity of the interface between the helium and hydrogen envelopes. The evolution is mostly in agreement with observations, but the high Hα velocities observed before $\sim$10 days for SN 2011dh are not reproduced by the model, which could again be related to our choice of initial conditions. The helium lines appear between 10 and 15 days near the photosphere and then evolve quite differently, where the He I 10830 Å velocity increases towards that of Hα, the He I 20581 Å velocity stays almost flat, and the He I 5876 Å and 6678 Å velocities decline. The evolution of the He I 10830 Å and 20581 Å velocities is in quite good agreement with observations, whereas the He I 5876 Å and 6678 Å velocities differ more.

As discussed (Sect. 3.1.3), the O I 7774 Å line appears later than in SN 2011dh, but the velocity evolution is otherwise similar, being rather flat at $\sim$6000 km/s. The evolution of the Fe II 5169 Å velocity follows that of the (Rosseland mean) continuum photosphere until $\sim$30 days, confirming the common assumption (e.g. E14) that this line is a good tracer of the photosphere during the diffusion phase. However, as mentioned before, this velocity is higher than observed for SN 2011dh, although the discrepancy disappears towards 150 days (see Fig. 9). It is worth noting that the Fe II 5169 Å velocity reaches a plateau near $\sim$6000 km s^{-1} at $\sim$40 days, a value close to the outer border of the inner helium envelope. This is a hint that the amount of Fe/Co/He material mixed into this part of the helium envelope could be too large, which in turn could force the photosphere to too high velocities.

3.3. Photometric evolution

Figure 12 shows the broad-band lightcurves for the standard model between 0 and 150 days as compared to observations of SN 2011dh. In agreement with observations, the maximum occurs at increasingly later times for redder bands and the drop onto the tail is more pronounced (deeper and faster) for bluer bands. Also in agreement with observations, the early (before 100 days) tail decline rates are generally higher for redder bands, with the J-band lightcurve having the steepest slope and the U-band lightcurve being almost flat. As has been noted in several sample studies (e.g. Taddia et al. 2015, 2017), the aforementioned behaviour of the maxima and the subsequent decline is shared not only by SN 2011dh, but by SE-SNe in general. It is also in agreement with the SE-SNe NLTE models presented by Dessart et al. (2015, 2016), and the lightcurves of the Type IIb model 3p65Ax1 are particularly similar to those of the standard model.

Although the overall agreement with observations is quite good, there are several differences between the model and the observations of SN 2011dh worth noting. Most notable are the differences in the U, J and K-bands and the evolution between

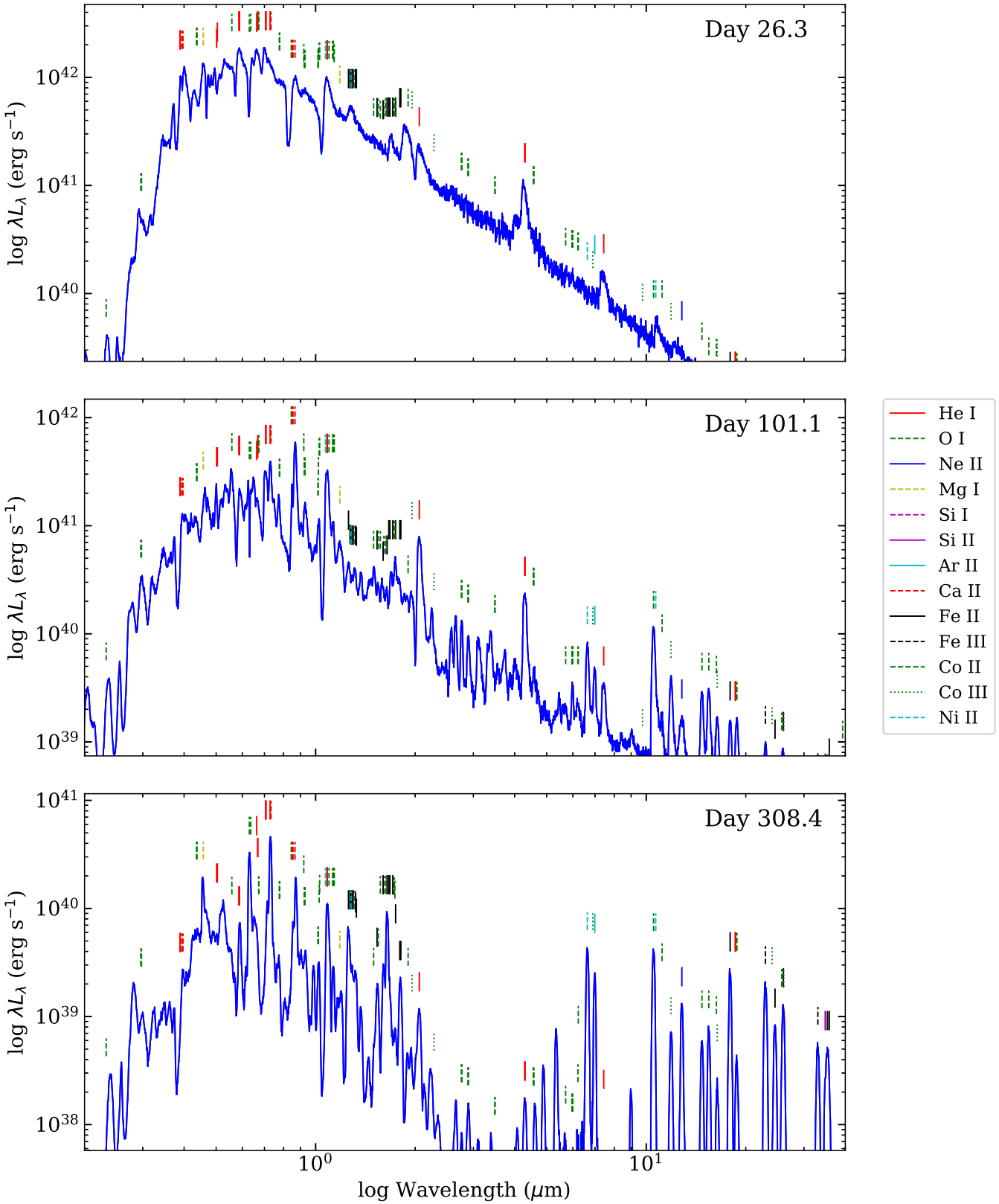

Fig. 10. Opical, NIR and MIR spectra for the standard model at 26 days (near peak), 101 days and at 308 days (nebular phase).

25 and 50 days, which is slower in R and bluer bands than observed for SN 2011dh. The growing discrepancy in the K-band could be related to dust formation in the ejecta (E15), and might suggest that this happens earlier than proposed in E15. Some of the discrepancy in the U-band could be explained by an un-

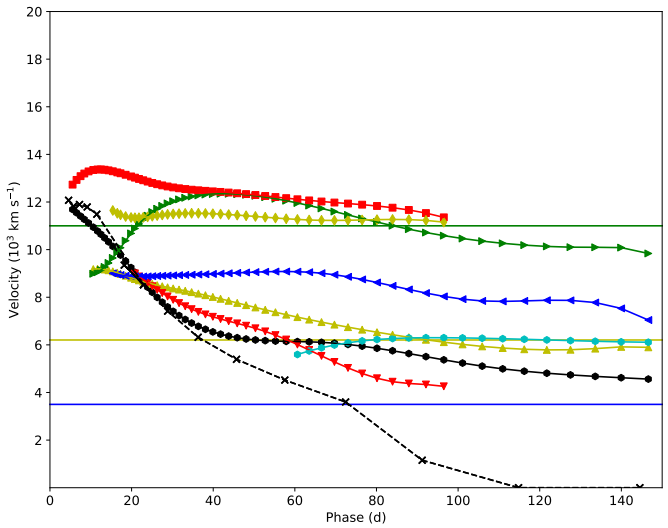

Fig. 11. Velocity evolution of the absorption minimum of the Hα (red squares), Hβ (yellow diamonds), He I 5876 Å (yellow upward triangles), He I 6678 Å (red downward triangles), He I 10830 Å (green rightward triangles), He I 20581 Å (blue leftward triangles), O I 7774 Å (cyan circles) and Fe II 5169 Å (black circles) lines for the standard model. The black crosses show the velocity evolution of the (Rosseland mean) continuum photosphere, whereas the horizontal lines mark the outer borders of the carbon-oxygen core (blue) and inner/outer (green/yellow) helium envelope.

derestimate of the extinction, but not all as the discrepancy is considerably larger on the tail than at peak.

3.4. Colour evolution

Figure 13 shows the intrinsic $U-V$, $B-V$, $V-I$ and $V-K$ colour evolution for the standard model between 0 and 100 days as compared to observations of SN 2011dh. Initially, we see a blueward trend in all colours reaching a minimum at ∼10 days. Subsequently all colours redden and reach a maximum at ∼40 days, in turn followed by a slow blueward trend for all colours, although the $V-I$ colour stays almost constant. This behaviour is in agreement with observations, although SN 2011dh does not show an initial blueward trend in the $U-V$ and $B-V$ colours, likely due to the influence of an initial cooling tail, not present in the model due to our choice of initial conditions.

As has been noted in several sample studies (e.g. Stritzinger et al. 2017), the properties of the colour evolution discussed here are shared not only by SN 2011dh, but by SE-SNe in general. They are also in agreement with the SE-SNe NLTE models presented by Dessart et al. (2015, 2016), and the colour evolution of the Type IIb model 3p65Ax1 is particularly similar to that of the standard model. As was noted for the lightcurve, the model evolution after ∼20 days is a bit slower than observed for SN 2011dh. The model $V-I$ and $U-V$ colours are bluer than observed for SN 2011dh, reflecting differences in the I- and U-bands.

3.5. Bolometric evolution

Figure 12 shows the pseudo-bolometric UV to MIR lightcurve for the standard model between 0 and 150 days as compared to observations of SN 2011dh. Similar to the comparison of the broad-band lightcurves, the model bolometric lightcurve is not

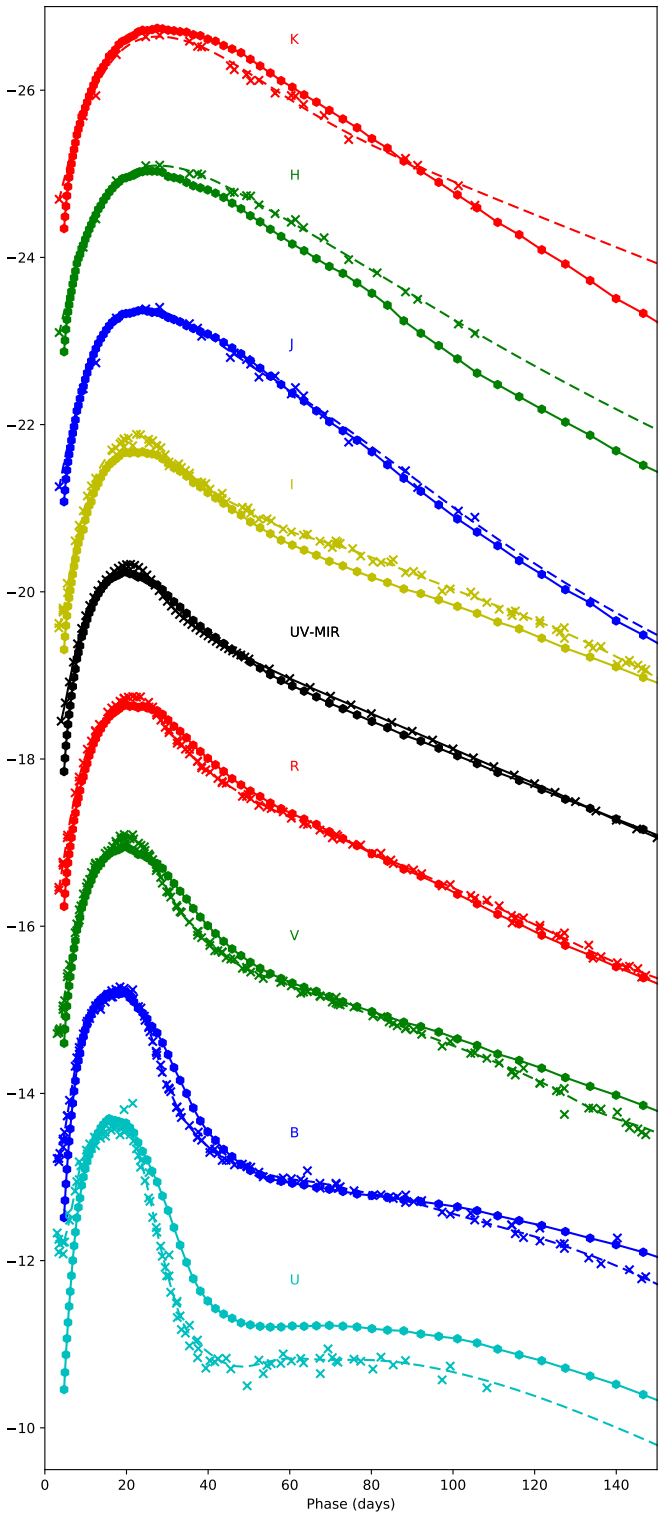

Fig. 12. Broadband and bolometric lightcurves for the standard model (solid lines and circles) compared to observations of SN 2011dh (dashed lines and crosses). From bottom to top we show the U (cyan), B (blue), V (green), R (red), UV to MIR pseudo-bolometric (black), I (yellow), J (blue), H (green) and K (red) lightcurves, which for clarity have been shifted with 2.6, 1.2, 0.0, -1.4, -3.5, -4.4, -5.8, -7.5, -8.9 mags, respectively.

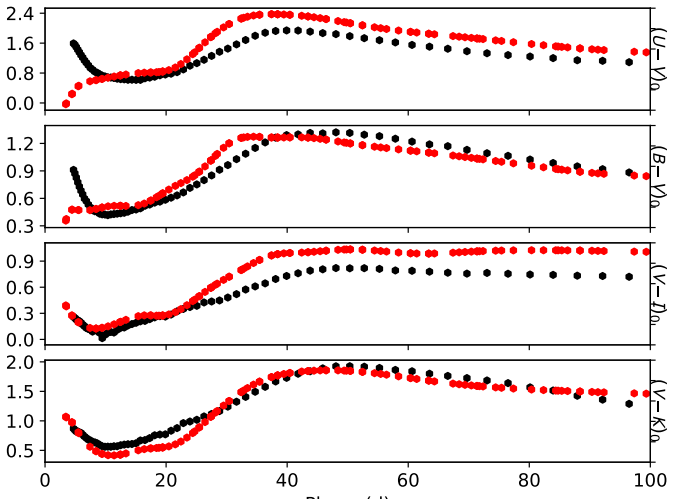

Fig. 13. $U-V$, $B-V$, $V-I$ and $V-K$ intrinsic colour evolution for the standard model (black) compared to observations of SN 2011dh (red).

a perfect match and is broader than the observed one. As the photospheric velocity is higher in the model (Sect. 3.2.1), this might indicate that a lower ejecta mass is needed. On the other hand, the mixing of the radioactive Fe/Co/He material plays a stronger role when non-thermal processes are taken into account (E18), and there are several indications (Sects. 3.1.3, 3.1.5 and 3.2.1) that the mixing may differ from that of SN 2011dh. We leave a further exploration of this, which would require a new grid of models to be constructed, for future work.

4. The effect of macroscopic mixing

Mixing of the SN ejecta occurs in the explosion due to hydrodynamical instabilities (e.g. Mueller et al. 1991), and is thought to take place on macroscopic scales only (e.g. Fryxell et al. 1991). The resulting 3-D structure is thereafter altered by the expansion of clumps containing radioactive material due to heating from radioactive decays. (e.g. Herant & Benz 1991). In JEKYLL, such macroscopically mixed ejecta is simulated through use of the virtual cell method (J11), where the compositional layers are assumed to be fragmented into spherical clumps, and mixed with each-other in an otherwise spherically symmetric ejecta. As JEKYLL is the only spectral-synthesis code that combines time-dependence, NLTE and a treatment of the macroscopic mixing, it is of great interest to investigate the effects of the macroscopic mixing on our results. To achieve this we compare the macroscopically mixed standard model presented in Sect. 3 with a microscopically mixed version of it, where the composition and density have been averaged in each spatial cell. To investigate the effects of the geometrical configuration of the clumps, we also explore a set of macroscopically mixed models differing in the expansion of the Fe/Co/He and Si/S clumps as well as the size of the clumps. The full set of models and their differences are described in Sect. 2.1. As we will see, the macroscopic mixing has several effects, both on the state of the matter and the radiative transfer, and in the latter case a geometrical aspect enters the problem. Below we discuss the effects on the state of the matter, the radiative transfer, the radioactive energy deposition, and the observed spectra and lightcurves. However, we begin with a discussion about the method used and its limitations.

4.1. Method and limitations

To simulate the macroscopic mixing JEKYLL use the virtual cell method (J11). The ejecta is assumed to be spherically symmetric on average, and the macroscopic mixing of it to be represented by distinct types of spherical clumps, characterized by their composition, density, size and filling factor (total fractional volume occupied). In the MC radiative transfer, the clumps are drawn based on their geometrical cross-section as the MC packets propagates through a macroscopically mixed region. This means that each MC packet sees a different geometrical arrangement of the clumps, which is justified in the limit of many clumps. The matter state is solved separately for each type of clumps using a MC radiation field constructed from MC packets passing through these clumps. The internal stratification of the matter state in the clumps is ignored, which is justified in the optically thin limit, and if the diffusion time is small compared to other relevant time-scales. When using the diffusion solver in the inner region, we assume the temperature to be the same in all types of clumps, which is justified if the diffusion time is small compared to other relevant time-scales. Note, that the MC radiative transfer for the γ-rays emitted in the radioactive decays uses the virtual cell method both in the inner and outer region.

Clearly, the virtual cell method is a simplification, and might be considered as an convenient parametrization of the more general 3-D problem. Although it would be possible to map a 3-D hydrodynamical simulation to this parametrization (and we may explore that path in the future), the models explored here are based on a 1-D hydrodynamical simulation by Woosley & Heger (2007), where the compositional layers have been artificially mixed into each-other (see Sect. 2.1). The extent of the mixing and, the size of the clumps and their filling factors have been chosen based on a combination of observational and theoretical arguments (see J15). In this work we explore the size of the clumps and their filling factors, which determines their 3-D configuration, but not the extent of the mixing. The constraints on these parameters are not very strong, and mainly apply to the core. Note, however, that the models without expansion of the Fe/Co/He and Si/S clumps and with 100 times more clumps are probably excluded by observations (see Ergon et al. (2015) for limits derived for SN 2011dh), and are merely useful to explore the effect of changing these parameters.

As JEKYLL is not hydrodynamical, we assume that all important hydrodynamical effects occurred before the start of the simulation. This assumption is safe with respect to the fragmentation of the ejecta into clumps, which occurs in the explosion, but less so for the subsequent expansion of the clumps due to heating from radioactive decays. At early times, the decay energy is deposited locally, and if the diffusion timescale is long compared to the decay and expansion timescales, this creates a temperature difference. If, in addition, the hydrodynamical timescale is small compared to the diffusion timescale, the corresponding pressure difference drives an expansion of the clumps. This means that we are on the safe side if the diffusion timescale is small compared to the decay and expansion timescales, or if the hydrodynamical timescale is large compared to the diffusion timescale. However, as mentioned, in the diffusion solver we assume a common temperature, so in the inner region the former requirement needs to be strictly satisfied. Fortunately, in all models, the diffusion time in the clumps never exceeds ~3 days in the core and ~0.5 days in the envelope, so after a few days the first condition is increasingly well fulfilled.

4.2. State of the matter

The different composition and density in the clumps as compared to microscopically mixed ejecta, gives rise to a different state of the matter, i.e. different populations of ionized and bound states and a different temperature. This, in turn, leads to different cooling/heating rates as well as different opacities and emissivities. Note, that the state of the matter depends on the radiation field and the radioactive energy deposition, but would be different even if those were the same as in the microscopically mixed model.

Fig. 14 shows the temperature and electron fraction in the different clump types in the core of the macroscopically mixed standard model as compared to the core of the microscopically mixed model. In the beginning the core is handled by the diffusion solver, which assumes the temperature to be the same in all clumps. The electron fraction differs, however, due to the different composition (and density) in the clumps. At ∼15 days, the core is handed over to the NLTE solver, and we see a small spread in the temperature. This indicates that the diffusion time is small but not negligible as compared to the decay and expansion timescales, in agreement with what was discussed above. After ∼50 days we see an increasing spread in the temperature, likely related to the different composition (and density) in the clumps. The spread in electron fraction remains large at all times.

One important effect of the clump density is that it changes the degree of ionization. This can be seen in Fig. 15, which shows the electron fraction in the Fe/Co/He and O/Ne/Mg clumps in the core for the macroscopically mixed models with and without expansion of the Fe/Co/He and Si/S clumps. As seen in the figure, the electron fraction is higher in the Fe/Co/He clumps and lower in the O/Ne/Mg clumps in the model with expanded Fe/Co/He and Si/S clumps, which is expected as the density is lower in the expanded Fe/Co/He clumps and higher in the compressed O/Ne/Mg clumps. A similar effect can bee seen in the helium envelope, in particular for the model with strong expansion of the Fe/Co/He clumps. Among other things, the degree of ionization affects the electron scattering opacity in the clumps, and we will discuss this issue more in the next section.

One important effect of the different composition in the clumps as compared to microscopically mixed ejecta is that strong coolants as e.g. calcium are distributed everywhere in microscopically mixed ejecta, and may overtake the cooling from other elements. This has particular importance in the nebular phase, and influence lines driven by collisional cooling as the [O I] 6300,6364 Å and [Ca II] 7291,7323 Å lines. This is illustrated by Fig. 16, where we show the net collisional cooling for these lines, as well as the total net collisional cooling for iron lines, in the core of the macroscopically mixed standard model and the microscopically mixed model. As seen in the figure, there is a strong difference between these models, and the net collisional cooling for the [Ca II] 7291,7323 Å line is much higher in the microscopically mixed model where calcium has been distributed everywhere. At the same time, the collisional cooling for the [O I] 6300,6364 Å line is much smaller in the microscopically mixed model, whereas the iron lines are less affected.

4.3. Radiative transfer

Except for the different state of the matter in the clumps, which affects the opacities and emissivities, the geometrical arrangement of these also affects the radiative transfer. In particular, it affects the diffusion time, which is governed by the mean free path. In a macroscopically mixed medium that is spherically symmetric on average (as is assumed in JEKYLL), and in the limit of many clumps, the mean free path can be expressed as an effective mean free path $\hat{\lambda}_\nu(r)$, which is an average over all random arrangements of the clumps (for a given geometrical configuration). In Appendix A we discuss the effective mean free path in more detail, and derive the diffusion approximation for such a medium in the case of a uniform radiation field (as is assumed in the diffusion solver), which only differs in that the Rosseland mean opacity is replaced by an effective Rosseland mean opacity based on the effective mean free path.

In general, the effective mean free path is complicated to calculate, and it is most straightforward to perform a MC calculation. In JEKYLL we use a MC method described in E18 and further discussed in Appendix A. Based on the effective mean free path we then calculate the effective Rosseland mean opacity, which is used by the diffusion solver in the inner region. In the outer region the geometrical effects are solved for implicitly by the MC radiative transfer, but we also calculate the effective Rosseland mean opacity for diagnostic purposes.

As shown in Appendix A, in the case of a uniform radiation field, there are a few important limiting cases in which the geometrical average of the mean free path simplify. First, in the limit of optically thin clumps, the effective opacity ($\hat{\kappa}_\nu = (\hat{\lambda}_\nu\,\rho)^{-1}$) is given by a *mass-average* of the opacity in the different clump types, and is independent of the geometry (i.e. the filling factors and the sizes of the clumps). Second, in the limit of optically thick clumps, the effective mean free path is given by a *volume-average* of the mean free path in the different clump types, and depends on both the geometry and the material opacity. Finally, in the limit of two distinct classes of clumps, one optically thick and one optically thin, the effective opacity depends *only* on the geometry, and is independent of the material opacity. This limit splits into two, depending on if the *geometrical mean free path*, i.e. the mean free path before hitting an optically thick clump, is longer or shorter than the size of the optically thin clumps. In the first case, which we call the clump limit, the effective mean free path is proportional to the geometrical mean free path. In the second case, which we call the bubble limit, the effective mean free path is proportional to the size of the optically thin clumps. As the mean free path in the optically thick clumps is zero, the effective mean free path is also proportional to the filling factor of the optically thin clumps. The geometrical limits are discussed further in Appendix A.

Armed with this knowledge we now turn to our models. Fig. 17 shows the effective Rosseland mean optical depth in the core for the full set of models. As seen in the figure, the effect of the macroscopic mixing is dramatic and the effective Rosseland mean opacity is almost ten times lower in the macroscopically mixed standard model than in the microscopically mixed model. This can be understood as early on the clumps are in the optically thick regime, and in this limit the effective mean free path is given by a volume average over the different clump types. The volume is dominated by the Fe/Co/He clumps which have expanded with a factor of 10 to reach a filling factor of 0.85. As the opacity in these clumps is broadly similar to that of the microscopically mixed core, the effective mean free path is ∼8.5 times longer, and the effective Rosseland mean opacity ∼8.5 times lower. In Appendix A we show that if the opacity is uniform and unaffected by the expansion, and one type of clumps have been expanded with a factor f_E to achieve a filling factor of Φ_E, the decrease of the effective opacity in the optically thick limit is given by

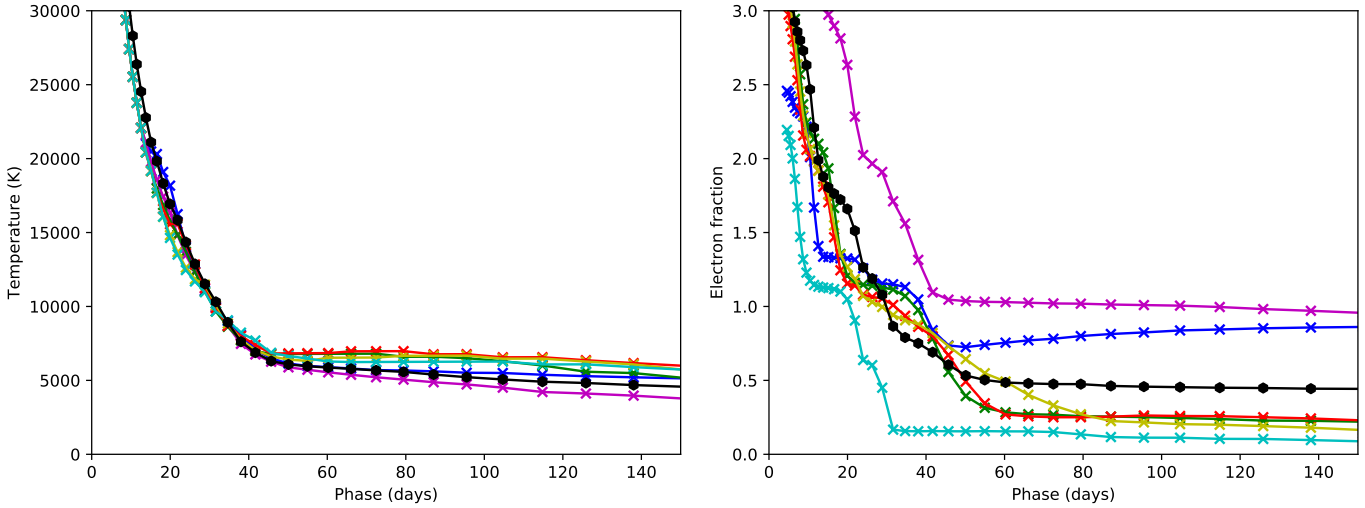

Fig. 14. Evolution of the temperature (left panel) and the electron fraction (right panel) in the Fe/Co/He (blue), Si/S (magenta), O/Si/S (green), O/Ne/Mg (red), O/C (yellow) and He/C (cyan) clumps in the core of the macroscopically mixed standard model as compared to the core of microscopically mixed model (black).

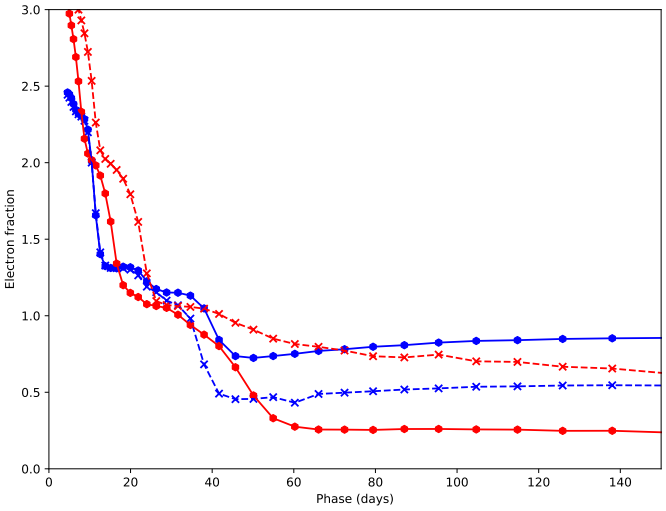

Fig. 15. Evolution of the electron fraction in the Fe/Co/He (blue) and O/Ne/Mg (red) clumps in the core of the macroscopically mixed models with (circles and solid lines) and without (crosses and dashed lines) expansion of the Fe/Co/He and Si/S clumps.

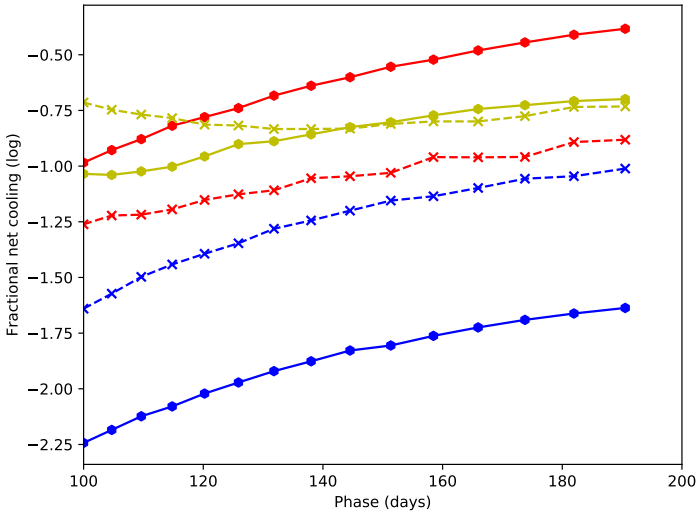

Fig. 16. Evolution of the (fractional) net collisional cooling in the nebular phase for the Fe lines (yellow) and the [O I] 6300,6364 Å (blue) and [Ca II] 7291,7323 Å (red) lines in the core for the macroscopically mixed standard model (crossed and dashed lines) as compared to the microscopically mixed model (circles and solid lines).

$$R = \frac{(1-\Phi_{\rm E})^2}{(1-\Phi_{\rm E}/f_{\rm E})} + \Phi_{\rm E}\, f_{\rm E} \qquad (1)$$

which gives $R \approx 8.5$, in agreement with above. If $\Phi_{\rm E}$ is large (as in our case), $R \approx \Phi_{\rm E}\, f_{\rm E}$, and if $\Phi_{\rm E}$ is small, $R \approx 1 + \Phi_{\rm E}\, f_{\rm E}$, which shows that a considerable decrease of the effective opacity can be achieved in a wide range of cases. After ∼40 days, the clumps gradually moves into the optically thin regime, and the geometrical effect on the effective Rosseland mean opacity disappears. However, as seen in the figure, the effective Rosseland mean opacity is still lower than that in the microscopically mixed model. This can be understood as in the optically thin limit the effective opacity is given by a mass-average over the different clump types. The mass is dominated by the oxygen-rich clumps, which due to compression have much higher density than in the macroscopically mixed model. As shown in Sect. 4.2, this leads to a lower degree of ionization and therefore to a lower electrons scattering opacity. This recombination effect, which occurs in the optically thin regime, is similar to the findings by Dessart et al. (2018), although in their work, the compressed clumps where surrounded by a void medium.

We no turn to the other models in our set, which are constructed to isolate the effects of the geometrical configuration. We first investigate the effect of the expansion of the Fe/Co/He and Si/S clumps on the effective Rosseland mean opacity. As seen in Fig. 17, if these are not expanded, the effective Rosseland mean opacity becomes much higher than in the standard model and more similar to that of the microscopically mixed model. This confirms our conclusion that the expansion of the Fe/Co/He clumps is the main reason for the lower Rosseland mean opacity. We then investigate the effect of the clump size on the effective Rosseland mean opacity. The clumps size is important because

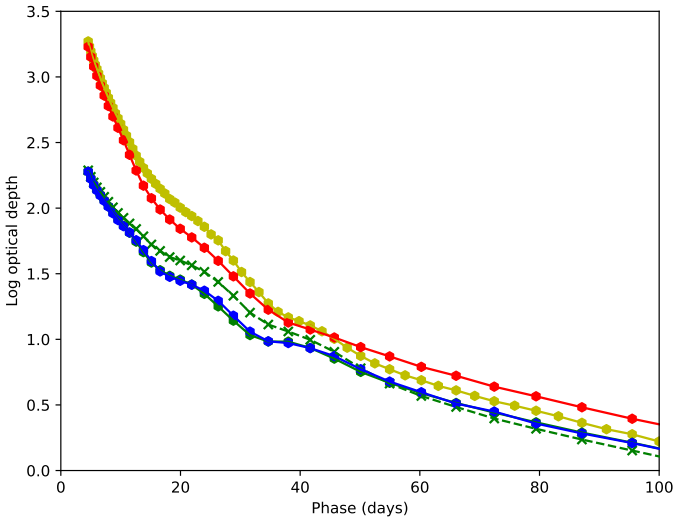

Fig. 17. Evolution of the Rosseland mean optical depth in the core for the macroscopically mixed standard model (blue circles) as compared to the microscopically mixed model (red circles). In addition, we show macroscopically mixed models with no expansion of the Fe/Co/He and Si/S clumps (yellow circles), and with strong expansion of the Fe/Co/He clumps in the helium envelope (green circles). Finally, we show a version on the latter model where the number of clumps have been increased with 100 times (green crosses).

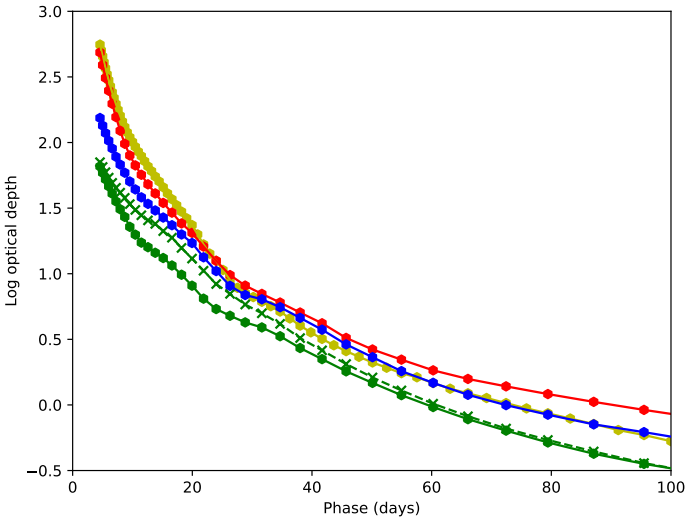

Fig. 18. Evolution of the Rosseland mean optical depth in the inner helium envelope for the macroscopically mixed standard model (blue circles) as compared to the microscopically mixed model (red circles). In addition, we show macroscopically mixed models with no expansion of the Fe/Co/He and Si/S clumps (yellow circles), and with additional expansion of the Fe/Co/He clumps in the helium envelope (green circles). Finally, we show a version of the latter model where the number of clumps have been increased with 100 times (green crosses).

if these are small enough we move into the optically thin regime. As seen in Fig. 17, if the number of clumps is increased with a factor of 100 (corresponding to $10^{3/2}$ times smaller clumps), the effective Rosseland mean opacity becomes considerably higher than in the standard model between ∼10 and ∼50 days. Before this, the clumps in both models are still in the optically thick regime, and after this, the clumps in both models have entered the optically thin regime.

The effect is similar in the inner helium envelope, where the Fe/He/Co clumps are mixed with helium-rich clumps, and Fig. 18 shows the effective Rosseland mean opacity for the full set of models. In the macroscopically mixed standard model the Fe/He/Co clumps in the inner helium envelope are expanded with a factor of 5, half of what is assumed in the core, and the effect on the Rosseland mean opacity is correspondingly smaller. However, in the model with strong (a factor of 8.5) expansion of these clumps, the effect is of similar magnitude as in the core. Note, that in this model, the effect on the degree of ionization in the helium-rich clumps from the compression is stronger than for the oxygen-rich clumps in the core. After the geometrical effect has disappeared, the effective Rosseland mean opacity is still a factor of ∼2 lower than in the microscopically mixed model. If the number of clumps are increased by a factor of hundred, we see a similar effect as in the core, and the effective opacity becomes considerably higher between ∼5 and ∼40 days.

The transition from the optically thick to the optically thin regime is illustrated by Fig. 18, where we show the effective Rosseland mean opacity for the model with strong expansion of the Fe/Co/He clumps in the helium envelope together with the corresponding optically thick and thin limits. We also show the geometrical clump and bubble limits, which are followed in cases when the optical depth difference between the clumps is high (see Appendix A). This is, however, not the case in our models, where the optical depth difference between Fe/He/Co and helium-rich clumps is quite modest (∼10). As seen in the figure, the effective Rosseland mean opacity initially follows the optically thick limit and begins to deviate at ∼5 days. During the transition it crosses, but do not follow, the geometrical limits and then gradually approaches and finally reaches the optically thin limit at ∼60 days. Note, that the difference between the optically thick and thin limit is modulated by the opacity in the clumps, which initially is higher in the helium-rich clumps due to a higher bound-free opacity, and then becomes lower due a lower electron scattering opacity. ,

In the figure we also show the effective Rosseland mean opacity for the model without expansion of the Fe/Co/He and Si/S clumps. This comparison shows that the decrease of the effective Rosseland mean opacity in the model where these clumps are expanded is dominated by the geometrical effect until ∼35 days, after which it is dominated by the decrease in material opacity in the helium-rich clumps due to the lower electron scattering opacity. These effects are complementary, and in general, the geometrical effect operates in the optically thick and transitional regimes, whereas the recombination effect operates in the optically thin regime. The geometrical effect is, however, potentially much stronger, although this requires that the sizes of the clumps are large enough to avoid the optically thin regime.

4.4. Radioactive energy deposition

In a macroscopically mixed model the radioactive decays occurs solely in the Fe/Co/He and Si/S clumps. The leptons emitted in the decays are assumed to deposit their energy locally, whereas the deposition of γ-ray energy depends on the radiative transfer. Early on, the Fe/Co/He and Si/S clumps are optically thick to the γ-rays and all the radioactive decay energy is deposited locally. When the Fe/Co/He and Si/S clumps approaches the optically thin regime, the γ-rays begin to leak out and may deposit their energy in other clumps. A discussed in Sect. 4.3, the radiative transfer in a macroscopically mixed model depends on the geometrical arrangement of the clumps, but once the optical depth of all clumps approaches zero, this dependence is lost and the ra-

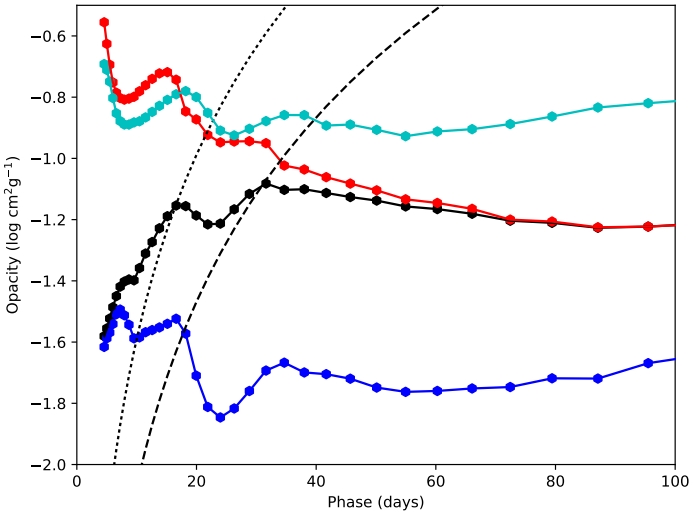

Fig. 19. Evolution of the Rosseland mean opacity in the inner helium envelope for the macroscopically mixed model with strong expansion of the Fe/He/Co clumps (black) and the corresponding Rosseland mean opacity in the limits of optically thick (blue) and thin (red) clumps. In addition, we show the geometrical clump (dashed black lines) and bubble (dotted black lime) limits and the evolution of the Rosseland mean opacity for the macroscopically mixed model without expansion of the Fe/Co/He and Si/S clumps (cyan).

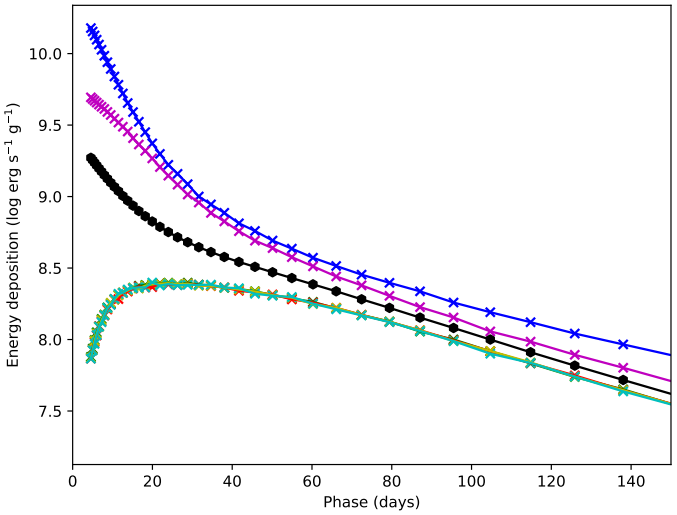

Fig. 20. Evolution of the radioactive energy deposition in the Fe/Co/He (blue), Si/S (magenta), O/Si/S (green), O/Ne/Mg (red), O/C (yellow) and He/C (cyan) clumps in the core of the macroscopically mixed standard model as compared to the core of the microscopically mixed model (black).

diative transfer is governed by the mass-averaged γ-ray opacity, which is the same as in a microscopically mixed model.

Fig. 20 shows the energy deposition in the different clump types in the core of the macroscopically mixed standard model as compared to the microscopically mixed model. As expected we se that the radioactive decay energy is almost solely deposited in the Fe/Co/He and Si/S clumps at early times. At ~10 days, the γ-rays begin to leak out from the Fe/Co/He and Si/S clumps and the energy deposition rises drastically in the other clumps. As time goes by the γ-ray energy deposition in the clumps approaches a common value. However, as the leptons still deposit their energy locally in the Fe/Co/He and Si/S clumps, the total radioactive energy deposition is allways higher in these. This difference increases with time as an increasing fraction of the γ-rays escape from the ejecta.

4.5. Observed spectra and lightcurves

We now turn to the observed lightcurves and spectra, and analyse what effect the macroscopic mixing have on these. We begin with the bolometric lightcurve, which is mainly affected by the effects on the radiative transfer discussed in Sect. 4.3, and then turn to the spectra, which are mainly affected by the effects on the state of the matter discussed in Sect. 4.2.

4.5.1. Bolometric lightcurves

Figure 21 shows the bolometric lightcurves for the full set of models. Compared to the microscopically mixed model, the peak of the bolometric lightcurve is brighter, occurs earlier and is considerably narrower for the macroscopically mixed standard model, which is exactly what we would expect from the lower effective Rosseland mean opacity in this model. Once on the tail, the difference disappears as the opacity difference decrease and the luminosity is anyway not determined by the diffusion time anymore. On the other hand, the bolometric lightcurve for the macroscopically mixed model without expansion of the Fe/Co/He and Si/S clumps, which has similar effective Rosseland mean opacity as the microscopically mixed model (Sect. 4.3), is almost identical to that of the microscopically mixed model. Clearly, the expansion of the Fe/Co/He and Si/S clumps may have a strong effect on the bolometric lightcurve through its influence on the effective Rosseland mean opacity. For the macroscopically mixed model with strong expansion of the Fe/Co/He clumps in the helium envelope the effect is quite dramatic, and the peak occurs almost 8 days before that of the microscopically mixed model and is much brighter. However, the effect also depends on the size of the clumps, and the bolometric lightcurve for same model with 100 times more clumps (which are therefore $10^{3/2}$ times smaller) is more similar to that of the macroscopically mixed standard model. As discussed in Sect. 4.3, the reason for this is that the geometrical effect on the effective Rosseland mean opcacity disappears when the clumps becomes optically thin. Unfortunately, no strong constraints exist on the size of the clumps and the expansion of the Fe/He/Co and Si/S clumps in the helium envelope, neither observational nor theoretical, and further work on this issue is highly warranted.

The effect of the macroscopic mixing on the lightcurves is not restricted to the case explored here, and will affect the lightcurves of stripped-envelope SNe in general. It may be stronger or weaker, depending on the expansion of the clumps containg radioactive material, the amount and distribution of such material, and the size of these and other clumps. However, if the clumps containing radioactive material are expanded with a large factor to fill a large fraction of the volume, it is potentlially dramatic (Sect. 4.3), as is examplified by the case explored here. The effect could lead to systematic underestimates of the ejecta masses of stripped-envelope SNe, as it is not included in codes commonly used to estimate these from the bolometric lightcurve. We note, however, that these codes does not include NLTE either, which at least for the Type IIb model explored here works in the opposite direction (E18). Recently, Dessart & Audit (2019) found a similar effect on the lightcurves Type II SNe using multi-D simulations with a simplified treatment of the matter. In these

simulations, the ejecta was assumed to consist of high density clumps surrounded by a lower density medium, but the density contrast was not directly linked to the expansion of radioactive material as in our models. The authors also introduce the concept of optically tick "macroclumps", and their qualitative discussion about their effect on the radiative transfer is in line with our discussion of the effective opacity in the limit of optically thick clumps. We note, however, that the concept of effective opacity presented here (Sect. 4.3 and Appendix A) is quite fruitful, as it allows us to quantify the effect of the macroscopic mixing on the radiative transfer. The MC method used in JEKYLL to calculate it may be incorporated also in tradiational non-MC codes, as e.g. diffusion-based hydrodynamical codes, commonly used to calculate the bolometric lightcurves of SNe.

4.5.2. Spectral evolution

Figure 22 shows the optical spectral evolution for the macroscopically mixed standard model compared to the microscopically mixed model. Initially the spectral evolution is very similar in the two models, but after ~40 days, they become increasingly different. In particular, the Ca II 8498,8542,8662 Å and [Ca II] 7291,7323 Å lines are much stronger, whereas the [O I] 6300,6363 Å line is much weaker in the microscopically mixed model. These lines are mainly driven by collisional cooling, and as discussed in Sect. 4.2, the net collisional cooling rates of the calcium lines are increased in the microscopically mixed model, whereas the net collisional cooling rate of the [O I] 6300,6363 Å line is decreased. As was previously pointed out by Fransson & Chevalier (1989), this is because calcium is a very effective coolant, and when calcium-rich material is mixed with other compositional zones it overtakes the cooling from other less efficient coolants. The difference in the [Ca II] 7291,7323 Å and [O I] 6300,6363 Å lines becomes very strong after ~100 days, and it is clear that macroscopic mixing needs to be taken into account, at least in the nebular phase, for the model to be realistic. This is particulerly true for the [O I] 6300,6363 Å line, given its importance to constrain the initial mass of the progenitor star (see e.g. Jerkstrand et al. 2015).

Figure 23 shows the optical spectral evolution for the macroscopically mixed standard model as compared to the model without expansion of the Fe/Co/He and Si/S clumps. Initially the spectral evolution is fairly similar, but after ~50 days a clear difference emerges in the Ca II 8498,8542,8662 Å line. The strongest difference is seen after ~80 days, where the line is much weaker in the model without expansion of the Fe/Co/He and Si/S clumps. The difference can be traced back to emission from the Si/S clumps in the core and the degree of ionization in these clumps, which is higher in the model with expanded Si/S clumps. As the Ca II 8498,8542,8662 Å line observed in SN 2011dh is in quite good agreement with that in standard model, this suggests that the expansion of the Si/S clumps in the core is considerable in SN 2011dh. This is in line with the findings in E15 based on the small-scale variations in the [O I] 6300,6364 and Mg I] 4571 Å lines, which suggests that the compression of the oxygen-rich clumps in the core is also considerable.

In Fig. 24 we show the full spectrum at 308 days for the same models as in Fig. 23. The most important difference is a change of ionization, as can be seen for especially the Mg I, Ca II, He I, Ne II and Fe III lines. As seen in the figure, several Fe III and Co III lines, which originates from the Fe/Co/He clumps in the core, show strong differences between the models with and without expansion of these clumps. There are also Fe II and Co II lines

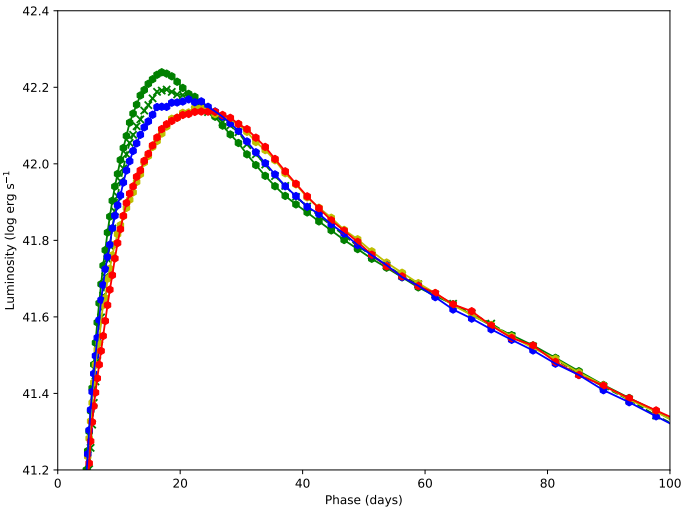

Fig. 21. Bolometric lightcurve for the macroscopically mixed standard model (blue circles) as compared to the microscopically mixed model (red circles). In addition, we show macroscopically mixed models with no expansion of the Fe/Co/He and Si/S clumps (yellow circles), and with strong expansion of the Fe/Co/He clumps in the helium envelope (green circles). Finally, we show a version of the latter model where the number of clumps have been increased with 100 times (green crosses).

available, so the (weak) temperature dependence in the Fe III and Co III line-stengths can be removed by using line-ratios between stage II and stage III lines. In addition, the models differ strongly in the Ne II 12.8 μm line, originating from O/Ne/Mg clumps in the core, as these clumps are compressed in the models with expanded Fe/Co/He and Si/S clumps. In order to better constrain the expansion of the Fe/He/Co clumps (as well as the compression of the O/Ne/Mg clumps), especially JWST to observe MIR spectra of Type IIb and other stripped-envelope SNe.

5. Conclusions

We use the new spectral synthesis code JEKYLL (E18) to evolve a macroscopically mixed Type IIb model from the photospheric to the nebular phase. The model belongs to a set of models presented in J15, and was shown to compare well with nebular observations of SN 2011dh in J15 and E15. Here we show that this model also reproduce the photospheric spectra and broadband lightcurves reasonably well. Some quantitative differences exist, however, and to find a model that improves the agreement is a challenge to be addressed in future work. Nevertheless, most important observational aspects of SN 2011dh, many of which are observed in other Type IIb SNe as well, are well reproduced by the model. This demonstrates that our understanding of Type IIb SNe has reached a rather mature level, and that NLTE modelling of such SNe is capable of producing realistic spectra and lightcurves, both in the photopsheric and nebular phase.

We also investigate the effects of the macroscopic mixing by comparing macroscopically and microscopically mixed models, and by varying the geometrical configuration in the macroscopically mixed models. In our treatment the geometrical configuration is parametrized by the size of the clumps and their filling factors, where the latter is determined by the expansion of the Fe/Co/He and Si/S clumps. In the nebular phase, we find strong effects on the collisional cooling rates in the macroscopically mixed regions, which affects the strength of lines driven by collisional cooling. For example, the 7291,7323 Å line is

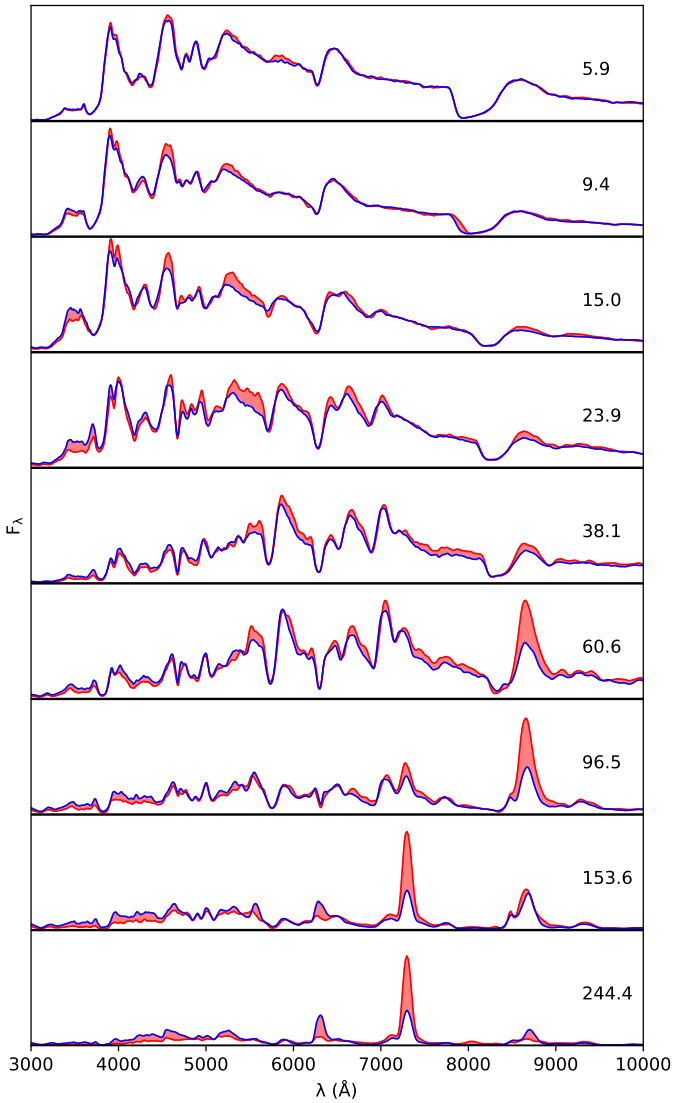

Fig. 22. Optical spectral evolution for the macroscopically mixed standard model (blue) as compared to the microscopically mixed model (red), where the difference has been highlighted in shaded red.

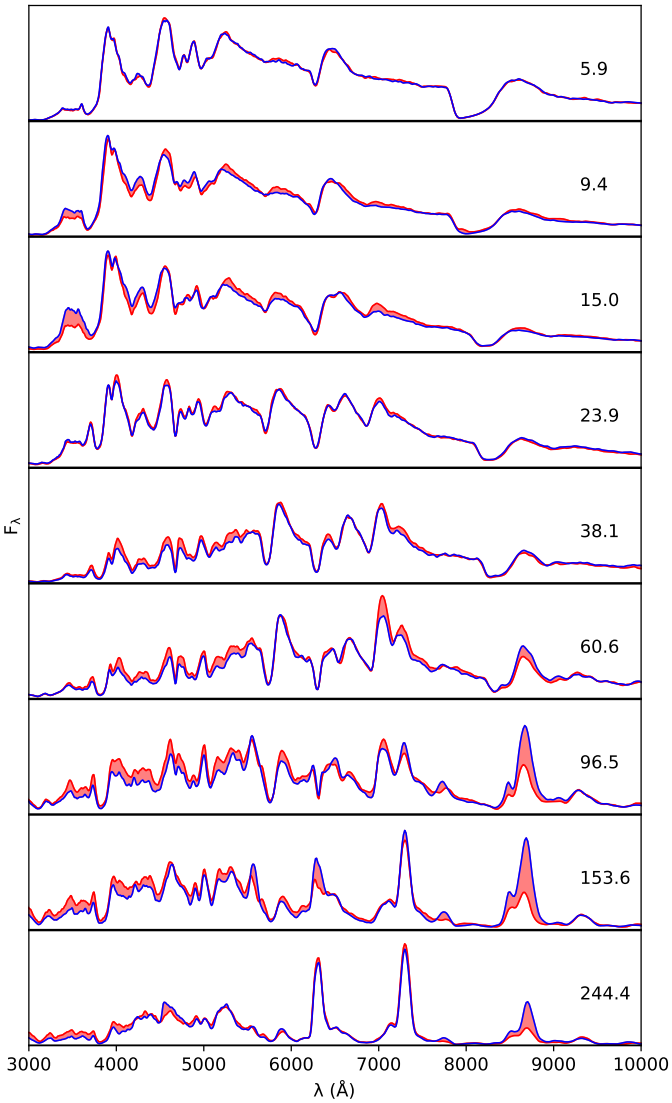

Fig. 23. Optical spectral evolution for the macroscopically mixed standard model (blue) as compared to the model without expansion of the Fe/C/He and Si/S clumps (red).

much weaker and the [O I] 6300,6364 Å, O I line much stronger in the macroscopically mixed case. The reason for this is that calcium, which is a very efficient coolant, overtakes the cooling from oxygen when the calcium- and oxygen-rich clumps are mixed together.

Early on, we find strong effects on the effective Rosseland mean opacity in the macroscopically mixed regions, which in turn affects the observed lightcurves. The diffusion peak of the bolometric lightcurve is considerably narrower in the macroscopically mixed case, and differs strongly if the Fe/Co/He clumps in the helium envelope are assumed to expand more than in our standard model. The effect is mainly geometrical, and is driven by the expansion of the Fe/Co/He and Si/S clumps, which creates a density contrast between these clumps and the rest of the ejecta. As we show, this always tends to decrease the effective opacity if the clumps are optically thick. In this limit, the geometrical effect on the effective Rosseland mean opacity is determined by the product of the filling factor Φ_E and expansion factor f_E of the expanded clumps. Assuming a uniform radiation field and a uniform opacity which is unaffected by the expansion, the decrease of the effective opacity can be quantified as $R = (1 - \Phi_E)^2/(1 - \Phi_E/f_E) + \Phi_E\ f_E$. The effect also depends on the typical clumps size, as it disappears when the clumps becomes optically thin. In addition to the geometrical effect, there is also a recombination effect, that tend to decrease the effective opacity in the limit of optically thin clumps, and which has been discussed by Dessart et al. (2018). These effects are complementary and operate in different regimes, but the geometrical effect is potentially stronger, and in our models it dominates.

The demonstrated effect of macroscopic mixing on the effective opacity has implications for lightcurve modelling of Type IIb SNe, as well as stripped-envelope SNe in general, and will tend to increase the estimated ejecta masses. It is therefore important to better constrain the expansion of the Fe/Co/He clumps and the typical size of these and other clumps. Constraints on the expansion/compression of the clumps can be obtained from spectra, and observations of the Ca II 8498,8542,8662 Å line suggests that the expansion of the Si/S clumps is considerable in SN 2011dh. More robust constraints on the expansion of the Fe/He/Co clumps can be derived from fine-structure lines in the

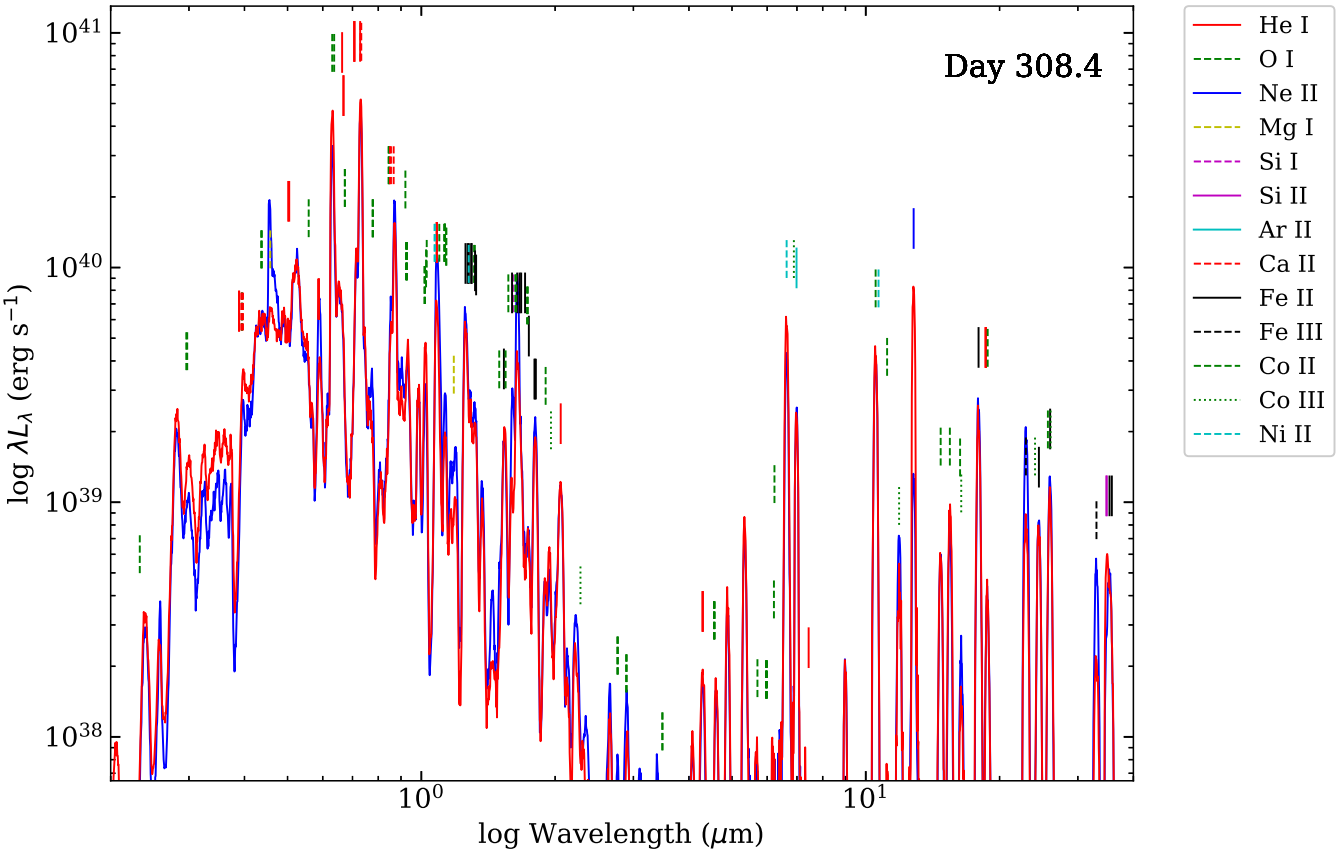

Fig. 24. Optical, NIR and MIR spectrum at 308 days (nebular phase) for the macroscopically mixed standard model (blue) as compared to the model without expansion of the Fe/C/He and Si/S clumps (red).

MIR, and we propose to use the JWST to observe the MIR spectrum of Type IIb and stripped-envelope SNe.

As was shown in E18, a full NLTE solution is required to reproduce the lightcurves and spectra of Type IIb SNe, and based on the findings in this work it is clear that *both* NLTE and macroscopic mixing are essential ingredients to reproduce the lightcurves and spectra of Type IIb SNe throughout their evolution.

Appendix A: Diffusion in a macroscopically mixed medium

Diffusion in a macroscopically mixed medium differs from that in a smooth medium due to the varying mean free path in the clumps. To understand and investigate the difference we begin by re-deriving the diffusion approximation for a smooth medium. Consider the energy transported through an area dA in time dt by photons with frequency ν originating from a distance l with energy density u_ν, propagating with polar direction θ and with a path-length distribution function f_ν. Using a Taylor expansion of u_ν this gives

$$dE_\nu = \frac{c}{2}\int_0^\pi\int_0^\infty f_\nu(l)\, u_\nu(r - l\,cos\,\theta)\, cos\,\theta\, sin\,\theta\, dl\, d\theta\, dA\, dt \approx \frac{c}{2}\int_0^\pi\int_0^\infty f_\nu(l)\, \frac{du_\nu}{dr}\, cos^2\,\theta\, sin\,\theta\, dl\, d\theta\, dA\, dt = \frac{\lambda_\nu c}{3}\frac{du_\nu}{dr}\, dA\, dt \quad \text{(A.1)}$$

Where λ_ν is the mean free path given by $\int_0^\infty f_\nu(l)\, l\, dl$. The flux is defined as $dE_\nu = F_\nu\, dA\, dt$ and integrating over frequency we get the general form of the diffusion approximation

$$F = \frac{c}{3}\int_0^\infty \lambda_\nu \frac{du_\nu}{dr} d\nu \quad \text{(A.2)}$$

Assuming a blackbody radiation field this can be written as

$$F = \frac{4acT^3}{3\kappa_R\rho}\frac{dT}{dr}, \quad \text{(A.3)}$$

where

$$\kappa_R = \int \frac{dB_\nu}{dT} d\nu \,/\, \int \lambda_\nu \frac{dB_\nu}{dT} d\nu \quad \text{(A.4)}$$

is the Rosseland mean opacity.

In a macroscopically mixed medium we need to sum the contributions from photons originating from each type of clumps with energy density $u_{\nu,i}$, filling factor Φ_i and effective path-length distribution function $\langle f_{\nu,i} \rangle$, which is an average of the path-length distribution function over all random geometrical arrangements of the clumps. In the following, we restrict ourselfs to the case when the energy density is the same in all types of clumps, which is what is assumed in the diffusion solver used in JEKYLL. In analogy with Eq. A.1 we the get

$$dE_\nu = \frac{c}{2} \sum \int_0^\pi \int_0^\infty \langle f_{\nu,i} \rangle \, u_\nu(r - l \, cos \, \theta) \, \Phi_i \, cos \, \theta \, sin \, \theta \, dl \, d\theta \, dA \, dt \approx \frac{\hat{\lambda}_\nu c}{3} \frac{du_\nu}{dr} \, dA \, dt \tag{A.5}$$

where $\hat{\lambda}_\nu$ is the effective mean free path given by

$$\hat{\lambda}_\nu = \sum \Phi_i \, \hat{\lambda}_{\nu,i} = \sum \Phi_i \int_0^\infty \langle f_{\nu,i} \rangle \, l \, dl \tag{A.6}$$

It is also convenient to define a corresponding effective opacity can by defined by $\hat{\kappa}_\nu = (\hat{\lambda}_\nu \, \rho)^{-1}$. In analogy with Eq. A.2 we then get the general form of the diffusion approximation in a macroscopically mixed medium

$$F = \frac{c}{3} \int_0^\infty \hat{\lambda}_\nu \frac{du_\nu}{dr} d\nu \tag{A.7}$$

and assuming a blackbody radiation field this can be written as

$$F = \frac{4acT^3}{3\hat{\kappa}_R \rho} \frac{dT}{dr}, \tag{A.8}$$

where

$$\hat{\kappa}_R = \int \frac{dB_\nu}{dT} d\nu \, / \int \hat{\lambda}_\nu \frac{dB_\nu}{dT} d\nu \tag{A.9}$$

is the effective Rosseland mean opacity in a macroscopically mixed medium. To calculate $\hat{\kappa}_R$ we need $\hat{\lambda}_\nu$ which in turn depends on $\langle f_{\nu,i} \rangle$. These geometrical averages of the path-length distribution functions can be written

$$\langle f_{\nu,i}(l) \rangle = \langle \exp(-\kappa_{\nu,i} \, \rho_i \, l_i) \prod_{j=0}^{n} \exp(-\kappa_{\nu,j} \, \rho_j \, l_j) \rangle = \int \cdots \int \exp(-\kappa_{\nu,i} \, \rho_i \, l_i) \prod_{j=0}^{n} \exp(-\kappa_{\nu,j} \, \rho_j \, l_j) f(l_i, ...l_n, l) \, dl_i \ldots dl_n \tag{A.10}$$

where i and j are the types of the originating and subsequent clumps, l_i and l_j are the (total) pathlengths through them, and $f(l_i, \ldots, \l_n, l)$ the corresponding distribution function at distance l. In general, calculating them is complicated, and in JEKYLL we use a MC method, which is is the same as used in the ordinary radiative transfer, except that the MC packets are terminated once an interaction with the matter is drawn.

However, there are a few limits, in which case the geometrical averages can be simplified. In the optically thin limit, the first exponential factor in Eq A.10 approaches one, the number of clumps traversed before absorption approaches infinity, and the (total) pathlength distribution function approaches a delta function at the average (total) pathlengths. As the probability for a point to lie within a clump of type j is just the filling factor, the average total path-length is $\Phi_j \, l$, and we get

$$\langle f_{\nu,i}(l) \rangle \approx \prod_{j=0}^{n} \exp(-\Phi_j \, \kappa_{\nu,j} \, \rho_j \, l) = \exp(-\sum_{j=0}^{n} \Phi_j \, \kappa_{\nu,j} \, \rho_j \, l) = \exp(-\overline{\kappa_\nu} \, \rho \, l) \tag{A.11}$$

where $\overline{\kappa_\nu}$ is a mass average of the opacity over the different clump types. Therefore, in this limit, the effective mean free path is given by

$$\hat{\lambda}_\nu = \frac{1}{\rho \, \overline{\kappa_\nu}} \tag{A.12}$$

In the optically thick limit, all photons are absorbed in the originating clump, and we get

$$\langle f_{\nu,i}(l) \rangle \approx \exp(-\kappa_{\nu,i} \, \rho \, l) \tag{A.13}$$

Therefore, in the optically thick limit the effective mean free path is given by

$$\hat{\lambda}_\nu = \sum \Phi_i \, \lambda_{\nu,i}, \tag{A.14}$$

a volume average of the mean free path over the different clump types. Using Eqs. A.12 and A.14, the ratio between the effective mean free path in the optically thick and thin limit (or equivalently, the ratio between the effective opacity in the optically thin and thick limit) can be expressed as

$$R_\nu = \sum \Phi_i \lambda_{\nu,i} \sum \Phi_j \frac{1}{\lambda_{\nu,j}} = \sum \sum \Phi_i \Phi_j \frac{\lambda_{\nu,i}}{\lambda_{\nu,j}} \geq 1 \tag{A.15}$$

where the last condition follows from the fact that $\lambda_{\nu,i}/\lambda_{\nu,j} + \lambda_{\nu,j}/\lambda_{\nu,i} \geq 2$. So the effective mean free path is the same in both limits only if the mean free path is the same in all clump types, and is otherwise longer in the optically thick limit. Note, that for medium with equal opacity in all clumps, Eq. A.15 can be expressed as

$$R_\nu = \sum \sum \Phi_i \Phi_j \frac{\rho_i}{\rho_j} \geq 1 \tag{A.16}$$

So in this case, the effective mean free path is the same in both limits only if the density is the same for all clump types, and is otherwise longer in the optically thick limit. In other words, the effective mean free path is increased and the effective opacity decreased by density variations.

A third limiting case is when one class of clumps are in the optically thick regime and anothor class of clumps are in the optically thin regime. When the optical depth approaches infinity in the optically thick clumps and zero in the optically thin clumps, the exponential factors in Eq. A.10 becomes either one

or zero. In particular, the product of the exponentials factors corresponding to optically thick clumps is only non-zero when the total path-length through those equals zero. As can be understood, if the path begin in an optically thin clump, the integral then corresponds to the distribution function of *not* hitting an optically thick clump at distance l. In anology with the material opacity, we then get

$$\langle f_{\nu,i}(l)\rangle = \exp(-\kappa_G\,\rho\,l) \tag{A.17}$$

where $\kappa_G\,\rho$ is the geometrical cross-section per volume produced by the optically thick clumps and κ_G the corresponding geometrical opacity. If the path begins in a optically thick clump, $\langle f_{\nu,i}(l)\rangle$ becomes a delta function a zero pathlength, and does not contribute to the effective mean free path. Therefore, we get

$$\hat{\lambda}_\nu = \sum \Phi_i/(\kappa_G\,\rho), \tag{A.18}$$

Where i corresponds to the optically thin clumps. Note, however that the derivation above assumes that $l \gg \langle l_i\rangle$, as the photons can not hit an optically thick clump until they have escaped the originating optically thin clump. In other words, it requires that the geometrical mean free path is much larger than the size of optically thin clumps. If the geometrical mean free path is much smaller than the size of the optically thin clumps, the effective mean free path is instead determined by the size of the optically thin clumps, and is given by

$$\hat{\lambda}_\nu = \sum \Phi_i\,\langle l_i\rangle, \tag{A.19}$$

Where i corresponds to the optically thin clumps. The geometrical limit therefore splits in two, one which we refer to as the clump limit, where $l_G \gg \langle l_i\rangle$ and the effective mean free path is given Eq. A.18, and one which we refer to as the bubble limit, where $l_G \ll \langle l_i\rangle$ and the effective mean free path is given by Eq. A.19. Following this we classify macroscopically mixed media with a high optical depth difference between the clumps as clump-like or bubble-like, depending on if the geometrical mean free path is smaller or larger than the average size of the low-optical-depth clumps.

The limits discussed are illustrated by Figs. A.1 and A.2, where we show the effective opacity for homologously expanding clump and bubble-like media consisting of high and low density clumps of equal grey opacity. The effective opacity was calculated with the same MC method as used in JEKYLL, and the limits using the expressions derived above. For the cump-like case shown in Fig. A.1 the clumps have equal size and the high density clumps a filling factor of 0.1. The optical depth differs by a factor of 1000 and the geometrical mean free path is ∼15 times larger than the size of the low density clumps. For the bubble-like case shown in Fig. A.2 the low density clumps are 20 times larger and have a filling factor of 0.1. The optical depth differs by a factor 100 and the geometrical mean free path is ∼15 times smaller than the size of the low density clumps. As seen in the figures, in the clump/bubble-like case, the effective opacity follows the optically thick limit until the clump/bubble limit exceeds the optically thick limit. The effective opacity then temporary moves into the clump/bubble limit, where the opacity is only determined by the geometry, follows this path until the clump/bubble limit exceeds the optically thin limit, and then moves into the optically thin limit.

Finally, lets explore a case more similar to the SN models in this work. Beginning with a smooth medium with constant grey opacity we divide it in two types of clumps of the same size and with filling factors 0.9 and 0.1. We then expand the latter (while keeping the density constant) with a factor of 9 to achieve a filling factor of 0.9. This is in line with the values for the Fe/He/Co zone in the core in the macroscopically mixed standard model. The optical depth differs by a factor of ∼20 and the geometrical mean free path is ∼3 times larger than the size of the low-density clumps, so the medium is modestly clump-like. The calculated effective opacity and the corresponding limits are shown in Fig. A.3, and as seen, during the transition from the optically

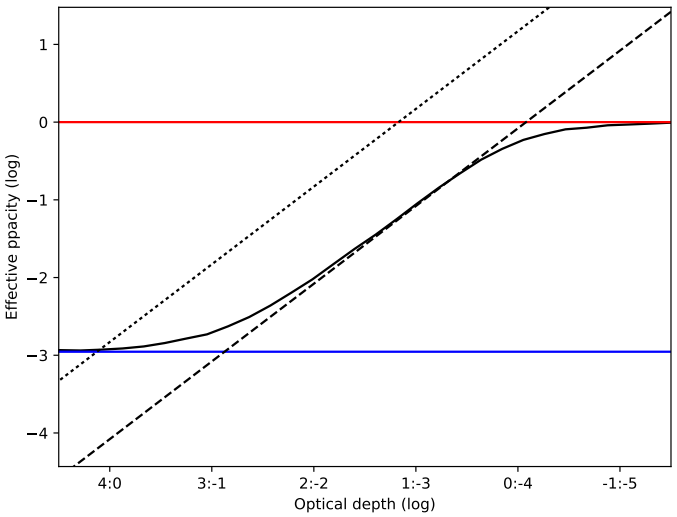

Fig. A.1. Effective opacity (black) for a homologously expanding clump-like medium with high and low density clumps of equal size and opacity, where the high density clumps have a filling factor of 0.1. We also show the optically thin (blue), optically thick (red) and geometrical clump (dashed black) and bubble (dotted black) limits. The opacity is given in arbitrary units, and the optical depth as H:L, where H and L are the optical depths in the high and low density clumps, respectively.

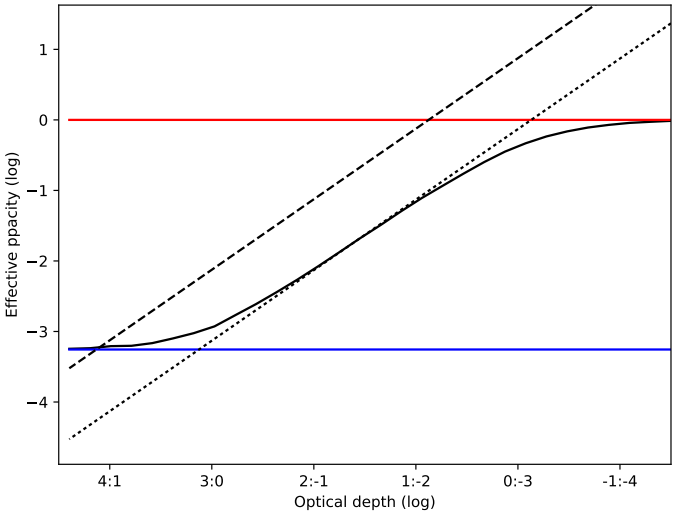

Fig. A.2. Effective opacity (black) for a homologously expanding bubble-like medium with high and low density clumps of equal opacity, where the low density clumps have a filling factor of 0.1 and are 20 times larger. We also show the optically thin (blue), optically thick (red) and geometrical clump (dashed black) and bubble (dotted black) limits. The opacity is given in arbitrary units, and the optical depth as H:L, where H and L are the optical depths in the high and low density clumps, respectively.

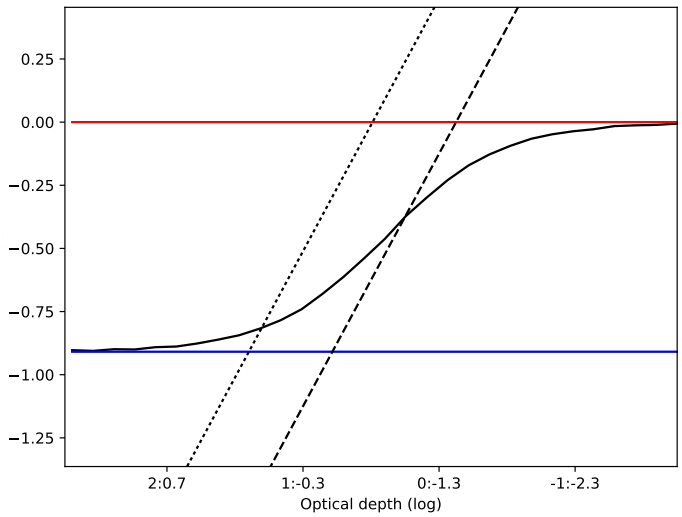

Fig. A.3. Effective opacity (black) for a homologously expanding medium with two types of clumps of equal mass and filling factors 0.9 and 0.1, where the latter have been expanded with a factor of 9. We also show the optically thin (blue), optically thick (red) and geometrical clump (dashed black) and bubble (dotted black) limits. The opacity is given in arbitrary units, and the optical depth as H:L, where H and L are the optical depths in the high and low density clumps, respectively.

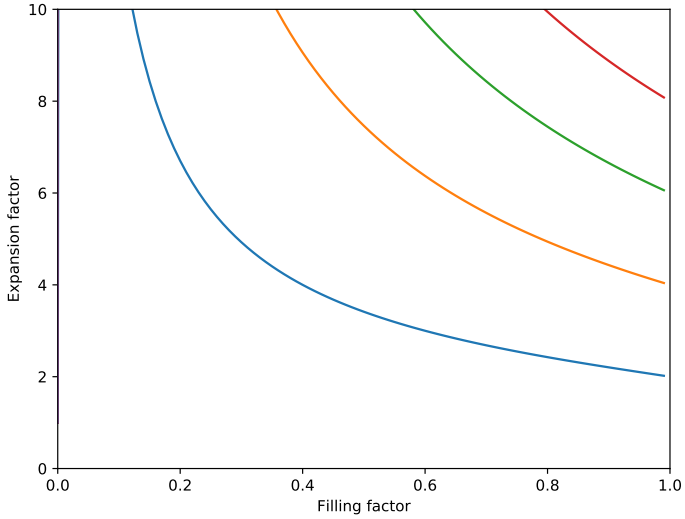

Fig. A.4. Effective opacity decrease in medium with uniform grey opacity, where one type of clumps have been expanded with a factor $f_{\rm E}$ to reach filling factor of Φ_E. Contours are shown for a decrease of the effective opacity with a factor of 2 (red), 4 (green), 6 (blue), and 8 (yellow).

thick to the optically thin limit the effective opacity crosses both geometrical limits but does not follow any of them, although it is a bit skewed towards the clumps limit. In the optically thin limit, the effective opacity equals that of a smooth medium, but from Eq. A.16 we see that in the optically thick limit it decreases by a factor

$$R = \Phi_{\rm C}/f_{\rm C} + \Phi_{\rm E}\, f_{\rm E} = \frac{(1-\Phi_{\rm E})^2}{(1-\Phi_{\rm E}/f_{\rm E})} + \Phi_{\rm E}\, f_{\rm E} \qquad \text{(A.20)}$$

where $f_{\rm C}$ is the compression factor for the high density clumps, $f_{\rm E}$ the expansion factor for the low density clumps, and we have used $\Phi_{\rm C} = 1 - \Phi_{\rm E}$ and $f_{\rm C} = (1 - \Phi_{\rm E}/f_{\rm E})/(1 - \Phi_{\rm E})$. This gives a decrease of the effective opacity with factor of 9 for the numbers given in this example. The general dependence of the opacity decrease in the optically thick limit on the filling factor and expansion factor of the low density clumps is illustrated in Fig. A.4. From Eq. A.20 we see that the effective opacity can not decrease more than the clumps have been expanded. If the filling factor for the expanded clumps is large ($\Phi_{\rm E} \approx 1$), the opacity decrease is given by $\Phi_{\rm E}\, f_{\rm E}$, and if it is small ($\Phi_{\rm E} \approx 0$) by $1 + \Phi_{\rm E}\, f_{\rm E}$.

References

Aldering, G., Humphreys, R. M., & Richmond, M. 1994, AJ, 107, 662
Bersten, M. C., Benvenuto, O. G., Nomoto, K., et al. 2012, ApJ, 757, 31
Dessart, L. & Audit, E. 2019, A&A, 629, A17
Dessart, L., Hillier, D. J., Li, C., & Woosley, S. 2012, MNRAS, 424, 2139
Dessart, L., Hillier, D. J., & Wilk, K. D. 2018, A&A, 619, A30
Dessart, L., Hillier, D. J., Woosley, S., et al. 2015, MNRAS, 453, 2189
Dessart, L., Hillier, D. J., Woosley, S., et al. 2016, MNRAS, 458, 1618
Ennis, J. A., Rudnick, L., Reach, W. T., et al. 2006, ApJ, 652, 376
Ergon, M. 2015, PhD thesis, Stockholm University
Ergon, M., Fransson, C., Jerkstrand, A., et al. 2018, A&A, 620, A156
Ergon, M., Jerkstrand, A., Sollerman, J., et al. 2015, A&A, 580, A142
Ergon, M., Sollerman, J., Fraser, M., et al. 2014, A&A, 562, A17
Fox, O. D., Azalee Bostroem, K., Van Dyk, S. D., et al. 2014, ApJ, 790, 17
Fransson, C. & Chevalier, R. A. 1989, ApJ, 343, 323
Fryxell, B., Mueller, E., & Arnett, D. 1991, ApJ, 367, 619
Herant, M. & Benz, W. 1991, ApJ, 370, L81
Jerkstrand, A., Ergon, M., Smartt, S. J., et al. 2015, A&A, 573, A12
Jerkstrand, A., Fransson, C., & Kozma, C. 2011, A&A, 530, A45
Liu, Y.-Q., Modjaz, M., Bianco, F. B., & Graur, O. 2016, ApJ, 827, 90
Lucy, L. B. 1991, ApJ, 383, 308
Marion, G. H., Vinko, J., Kirshner, R. P., et al. 2013, ArXiv e-prints
Maund, J. R., Fraser, M., Ergon, M., et al. 2011, ApJ, 739, L37
Maund, J. R., Smartt, S. J., Kudritzki, R. P., Podsiadlowski, P., & Gilmore, G. F. 2004, Nature, 427, 129
Mueller, E., Fryxell, B., & Arnett, D. 1991, A&A, 251, 505
Shigeyama, T., Suzuki, T., Kumagai, S., et al. 1994, ApJ, 420, 341
Shull, J. M. & van Steenberg, M. 1982, ApJS, 48, 95
Stritzinger, M. D., Taddia, F., Burns, C. R., et al. 2017, ArXiv e-prints
Taddia, F., Sollerman, J., Leloudas, G., et al. 2015, A&A, 574, A60
Taddia, F., Stritzinger, M. D., Bersten, M., et al. 2017, ArXiv e-prints
Wongwathanarat, A., Janka, H.-T., Müller, E., Pllumbi, E., & Wanajo, S. 2017, ApJ, 842, 13
Woosley, S. E., Eastman, R. G., Weaver, T. A., & Pinto, P. A. 1994, ApJ, 429, 300
Woosley, S. E. & Heger, A. 2007, Phys. Rep., 442, 269